Study of Sediment Transport in a Tidal Channel-Shoal System
Lateral Effects and Slack-Water Dynamics

Zhou, Zaiyang; Ge, Jianzhong; van Maren, D. S.; Wang, Zheng Bing; Kuai, Yu; Ding, Pingxing

DOI
10.1029/2020JC016334

Publication date
2021

Document Version
Final published version

Published in
Journal of Geophysical Research: Oceans

JGR Oceans

RESEARCH ARTICLE
10.1029/2020JC016334

Study of Sediment Transport in a Tidal Channel-Shoal System: Lateral Effects and Slack-Water Dynamics

Zaiyang Zhou[1,2], Jianzhong Ge[1,3], D. S. van Maren[1,2,4], Zheng Bing Wang[2,4], Yu Kuai[2], and Pingxing Ding[1]

[1]State Key Laboratory of Estuarine and Coastal Research, East China Normal University, Shanghai, China, [2]Faculty of Civil Engineering and Geosciences, Delft University of Technology, Delft, The Netherlands, [3]Institute of Eco-Chongming (IEC), ChenJiazhen, Shanghai, China, [4]Department of Marine and Coastal Systems, Deltares, Delft, The Netherlands

Abstract Lateral flows redistribute sediment and influence the morphodynamics of channel-shoal systems. However, our understanding of lateral transport of suspended sediment during high and low water slack is still fairly limited, especially in engineered estuaries. Human interventions such as dike-groyne structures influence lateral exchange mechanisms. The present study aims to unravel these mechanisms in a heavily engineered, turbid channel-shoal system in the Changjiang Estuary, using a high-resolution unstructured-grid three-dimensional model and in situ observations. Analysis of model results reveals two typical transport patterns during slack-water conditions, that is, shoal-to-channel transport during low water slack and channel-to-shoal transport during high water slack. A momentum balance analysis is carried out to explain mechanisms driving the lateral transport of suspended sediment during high water slack, revealing the importance of lateral pressure gradients, Coriolis force, and the curvature-induced term. Groyne fields play a crucial role in sediment transport, especially during low water slack. A model scenario in which one groyne is removed reveals that groyne fields strongly influence lateral sediment transport. The decomposition of the sediment transport flux reveals that the turbidity maximum is shaped by a balance between seaward advection by residual flows, and landward transport by tidal pumping and gravitational circulation. Within the turbidity maximum, sediment is laterally redistributed by lateral flows during slack-water conditions, greatly influencing estuarine channel morphology.

Plain Language Summary Sediment deposition in navigation channels requires regular maintenance dredging. To minimize channel siltation, in-depth knowledge of transport mechanisms and the effect of mitigation measures (such as groyne fields) is needed. These mechanisms include both longitudinal (along-channel) and lateral (cross-channel) processes. It is now well established that longitudinal processes play a key role in sediment convergence. However, during high and low water slack when the longitudinal velocity is small, lateral transport of suspended sediment becomes more important. These lateral transport mechanisms have a large influence on channel morphology. In this study, we investigate longitudinal and lateral transport of suspended sediment with a numerical model, revealing two typical lateral sediment transport patterns during high and low water slack which greatly influence the exchange of sediment between the channel and the shoals. The model also demonstrates the effect of groyne fields on lateral sediment transport. These findings expand our understanding of sediment transport in channel-shoal systems in general, but in engineered systems in particular.

Key Points:

- During stratified slack-water conditions, the lateral pressure gradients drive sediment transport between the shoal and the main channel
- Longitudinal sediment convergence primarily results from advection, tidal pumping, and longitudinal vertical circulation
- Lateral transport of suspended sediment and distribution patterns are influenced by groynes

Correspondence to:
J. Ge,
jzge@sklec.ecnu.edu.cn

Citation:
Zhou, Z., Ge, J., van Maren, D. S., Wang, Z. B., Kuai, Y., & Ding, P. (2021). Study of sediment transport in a tidal channel-shoal system: Lateral effects and slack-water dynamics. *Journal of Geophysical Research: Oceans*, *126*, e2020JC016334. https://doi.org/10.1029/2020JC016334

Received 25 APR 2020
Accepted 17 FEB 2021

1. Introduction

Sediment transport in estuaries directly influences the bed level which in turn impacts the navigability of shipping channels. Sediment dynamics also influence estuarine ecology, for instance through water clarity (and therefore primary production, providing the base of the food chain) and habitat suitability (especially on the intertidal areas)—see Wood (1997). In many systems worldwide, estuarine sediment dynamics are increasingly modified by changes in river and sediment discharges (Guo et al., 2018; Syvitski, 2005; Walling & Fang, 2003) or more local interventions (Wang et al., 2015), requiring a thorough understanding of transport processes.

The estuarine suspended sediment concentration (SSC) is highest in the Estuarine Turbidity Maximum (ETM). ETMs result from longitudinal (along-channel) sediment convergence, i.e., converging sediment transport generated by combined effects of residual estuarine circulation, tidal dynamics, and sediment erosion and deposition (Dyer, 1988; Officer, 1981). Estuarine circulation is the combined effect of gravitational circulation (Postma, 1967), internal tidal asymmetry (Jay & Musiak, 1994) due to tidal straining (Simpson et al., 1990), lateral tidal residual flows (Lerczak & Geyer, 2004), and river flow; the relative importance of each component is highly variable. Residual transport by time lag effects, such as settling lag and scour lag (Postma, 1961), is the result of sediment properties (settling velocity, critical shear stress for erosion) in combination with asymmetries in the hydrodynamics (time-varying or spatial asymmetries). ETMs are abundant worldwide, and have been studied in great detail—see de Nijs and Pietrzak (2012), McSweeney et al. (2016), or Burchard et al. (2018) for examples and more detailed references. Nevertheless, sediment transport in systems that have complex ETM dynamics or extremely high SSC, especially when strongly influenced by groyne fields, is still poorly understood. Ralston et al. (2012) demonstrated through use of in situ observations and a numerical model that the sediment flux in a channel-shoal system can be strongly laterally segregated. The shoals can serve as pathways for seaward sediment flux and the channel can support the landward flux. However, this laterally varying, longitudinal transport pattern may differ substantially in channel-shoal systems which are impacted by dikes and groynes, e.g., the North Passage of the Changjiang Estuary.

In addition, the role of lateral flows (cross-channel flows) in sediment transport is increasingly recognized. Although lateral flow normally has a much smaller magnitude, its impact on momentum balance and transport of particles cannot be neglected (Dronkers, 1996; Lerczak & Geyer, 2004). Lateral flow, caused by lateral depth variation, channel curvature, and Coriolis acceleration among others, drives and traps sediment (Huijts et al., 2006). These mechanisms reinforce or counteract each other (Kim & Voulgaris, 2008), enhancing the complexity of lateral flow and sediment transport. Chen et al. (2009) used a hydrodynamic model to explore the influence of wind effect on lateral circulation in stratified and unstratified conditions. They concluded that the wind direction could change the direction of lateral sediment flux (from channel to shoals for down-estuary winds). Chen and de Swart (2018) concluded that the longitudinal variation of lateral flow drives trapping of sediment in the North Passage. Their work primarily addressed tide-averaged effects of lateral flow and lateral trapping of sediment. However, there is also a need to investigate the intratidal variation in sediment transport processes in greater detail.

Groynes are often constructed in the coastal zone (Kristensen et al., 2016; Scott et al., 2016), protecting shorelines from erosion problems. They are also widely applied in rivers, tidal inlets, and navigation channels to mitigate deposition problems. Most of our knowledge about groynes is primarily based on zero-density-gradient conditions. Ouillon and Dartus (1997) set up a three-dimensional model to simulate a shallow turbulent flow around a groyne in a rectangular channel. Uijttewaal et al. (2001) explored exchange process between a groyne field and the main stream in a riverine condition. They observed two types of exchange related to two-dimensional flow, and mentioned a small three-dimensional effect which could cause a net outward flow at the free surface. However, salinity-induced density gradients which are widespread in estuarine environments can greatly impact groyne-related three-dimensional effects, such as lateral circulation, stratification, and near-bed transport of high-concentration water mass. Zhou et al. (2019) reported that near-bed lateral flows were strengthened by retention of high-salinity water during ebb tides. This lateral flow greatly influenced lateral transport processes, as evidenced by a pronounced intratidal salinity variation near the deep channel. Nevertheless, our understanding of the effect of groyne fields in estuarine environments is still very limited. On the other hand, Luan et al. (2018) concluded that the existence of dikes and groynes caused attenuation of currents, decrease of bed shear stress, and enhanced deposition in the groyne-sheltered area. Therefore, the reported lateral flow and abundant deposition in the groyne-sheltered shoal jointly highlight a need for research on lateral transport of suspended sediment and effects of groynes.

The objective of the current work is therefore to quantify and analyze the influence of lateral flows, with attention to the effect of groynes on sediment transport. For this purpose, we investigated the North Passage of the Changjiang Estuary. The North Passage is very turbid, suffering from high siltation rates (Ge et al., 2018), and subject to lateral flows strengthened by an extensive groyne system (Zhou et al., 2019). Earlier work (Ge et al., 2018; Liu et al., 2011; Song et al., 2013) revealed the occurrence of fluid mud in

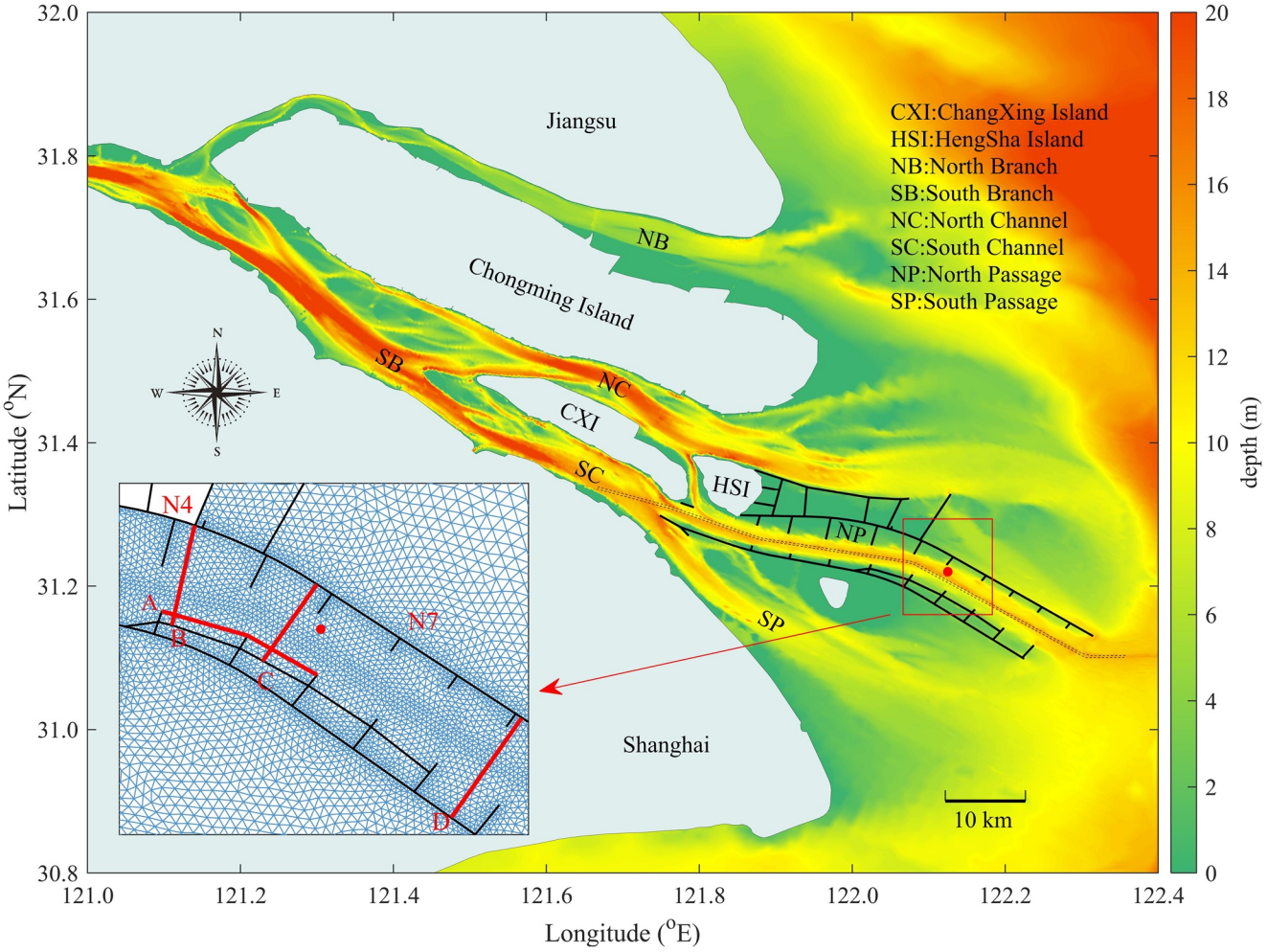

Figure 1. Bathymetry of the Changjiang Estuary and adjacent regions. Black lines in the river mouth represent dikes and groynes around the North Passage. Two dashed lines indicate the deep channel. Red dot indicates the measuring site. Zoomed-in subfigure shows the unstructured mesh used in the model and four red lines indicates four transects for further analysis. The measuring site is 2.26 km from the north dike, 1.05 km from the nearest groyne tip.

the Changjiang Estuary (particularly in the North Passage). Most of these earlier analyses are based on single-point observations which fail to capture the complex spatial dynamics of such high-concentration layers. Therefore, in this study, we use a sediment transport model, which is validated against field data collected using a tripod system, to investigate the lateral transport of suspended sediment. This paper is organized as follows. The study site, observational methods, and applied model are described in Section 2. The model results are presented in Section 3, followed by a more in-depth analysis of transport mechanisms (Section 4). Discussion and conclusions are summarized in Sections 5 and 6, respectively.

2. Study Site, Observational, and Numerical Method

2.1. Study Site

The North Passage is the main navigation channel among four outlets of the Changjiang Estuary (Figure 1). To enhance shipping capacity, the Deepwater Navigation Channel (DNC) project has been conducted in the North Passage. The depth of the main channel is maintained at 12.5 m and the channel is protected by combination of dikes and groynes (Ge et al., 2012). The DNC project includes two long dikes with 19 groynes attached to these two dikes. Before the DNC project, the water depth in the main channel was only about 7 m (below the local minimum theoretical tidal level, similarly hereinafter). The project has three phases and the channel has been deepened from 7 to 12.5 m (350–400 m in width) after all phases (Hu & Ding, 2009).

Impermeable dikes are designed near the mean tidal level to block the tidal current, and groynes are designed to increase flow velocity and maintain water depth in the channel (Ge et al., 2012). In summary, the design of this project has three aims: (1) increasing the water depth to fulfill the demand of ocean shipping (dredging and deepening), (2) preventing sediment transport into the North Passage (dikes), and (3) increasing sediment erosion in the main channel (groynes). In 2016, the south dike was heightened to about 1.9 m above the minimum theoretical tidal level. Most of the north dike was heightened to about 3.4 m above the minimum theoretical tidal level, which becomes a road nowadays. This supplementary engineering work significantly blocked the overtopping flow, making the North Passage a laterally closed system.

The North Passage suffers from extremely high siltation rates, varying between 60 and 80 million m^3/year (Wang et al., 2015). Large amounts of sediment also deposited in the relatively sheltered groyne fields, forming the present-day channel-shoal system. Most dredging work is conducted within the main channel of curved region between Groyne N4 and N7 (Figure 1). In 2016, about 35 million m^3 of fine sediment was dredged in this area and most of the sediment was used for land reclamation. The median grain size of suspended sediment is 7–11 μm (Guo & He, 2011). In the model used in this study, dikes and groynes are treated as "impermeable walls" which means there are no overtopping flows across these structures. This treatment of dikes and groynes is reasonable as the whole south dike has been heightened and most of the north dike has been heightened.

This channel-shoal system is affected by both fluvial and tidal forcing. According to data from the Datong Gauging Station, the average water discharge of the Changjiang River is about 40,000 m^3/s in the wet season, with the maximum exceeding 70,000 m^3/s, and about 10,000 m^3/s in the dry season. Reduction of sediment supply due to the upstream Three Gorges Dam (TGD) project is significant and its influences on morphodynamics are profound (Luan et al., 2016; Yang et al., 2014). Along the coast of the East China Sea, semidiurnal tides are dominant with a mean tidal range of about 2.7 m.

2.2. Observations

A tripod frame was deployed on the river bed (about 10 m below the local minimum theoretical tidal level) north to the deep channel in the North Passage (Figure 1). The tripod location (between the north shoal and the main channel) was determined by the aim of detecting channel-shoal sediment transport and exploring effects of groynes (north groynes are longer). The side slope of this location is about 1:1,000, indicating tripod observations will not be affected by the slope. The tripod integrated two RDI Acoustic Doppler Current Profilers (ADCPs), a Nortek Acoustic Doppler Vector (ADV), a Point Current Meter (ALEC, JFE ALEC Co., Ltd, Japan), a Tide/wave Logger (RBR, RBR Ltd., Canada), a Conductivity, Temperature, and Pressure Recorder (CTD, Sea-Bird Electronics, Inc., USA), and an Optical Backscattering Sensor (OBS, D&A Instruments CO, type: 3A, USA). The height of OBS turbidity sensor was 0.9 m above the bed and the temporal resolution was 100 s. Water turbidity detected by the OBS was calibrated to acquire suspended sediment concentration (SSC) at our laboratory with sediment samples collected at the measuring site. The same calibration process was introduced in detail in Ge et al. (2018). Caution should be taken if the OBS is used in an extremely high SSC environment (this limit depends on the performance of a specific OBS and can be found during the calibration), which may cause ambiguity problem at concentrations exceeding 10 g/L (i.e., a low optical output could mean a low or high concentration). However, this problem did not exist during our observation as the maximum SSC was up to 10 g/L, and the relation between OBS output and SSC can be described by a piecewise regression function. Detailed configuration of this tripod observation can be found in Zhou et al. (2019).

Data collected by the tripod (Figure 2) included water levels, single-point current velocity (decomposed in along-channel and cross-channel directions), near-bed salinity, and SSC collected over a 12-day period starting from December 6, 2016 (abbreviated as 12/06). The whole observation was divided into three phases (Figure 2f) based on hydrodynamic conditions: Phase A represents neap tidal conditions (12/07–12/11), Phase B represents intermediate tidal conditions (12/11–12/14), and Phase C represents spring tidal conditions (12/14–12/18).

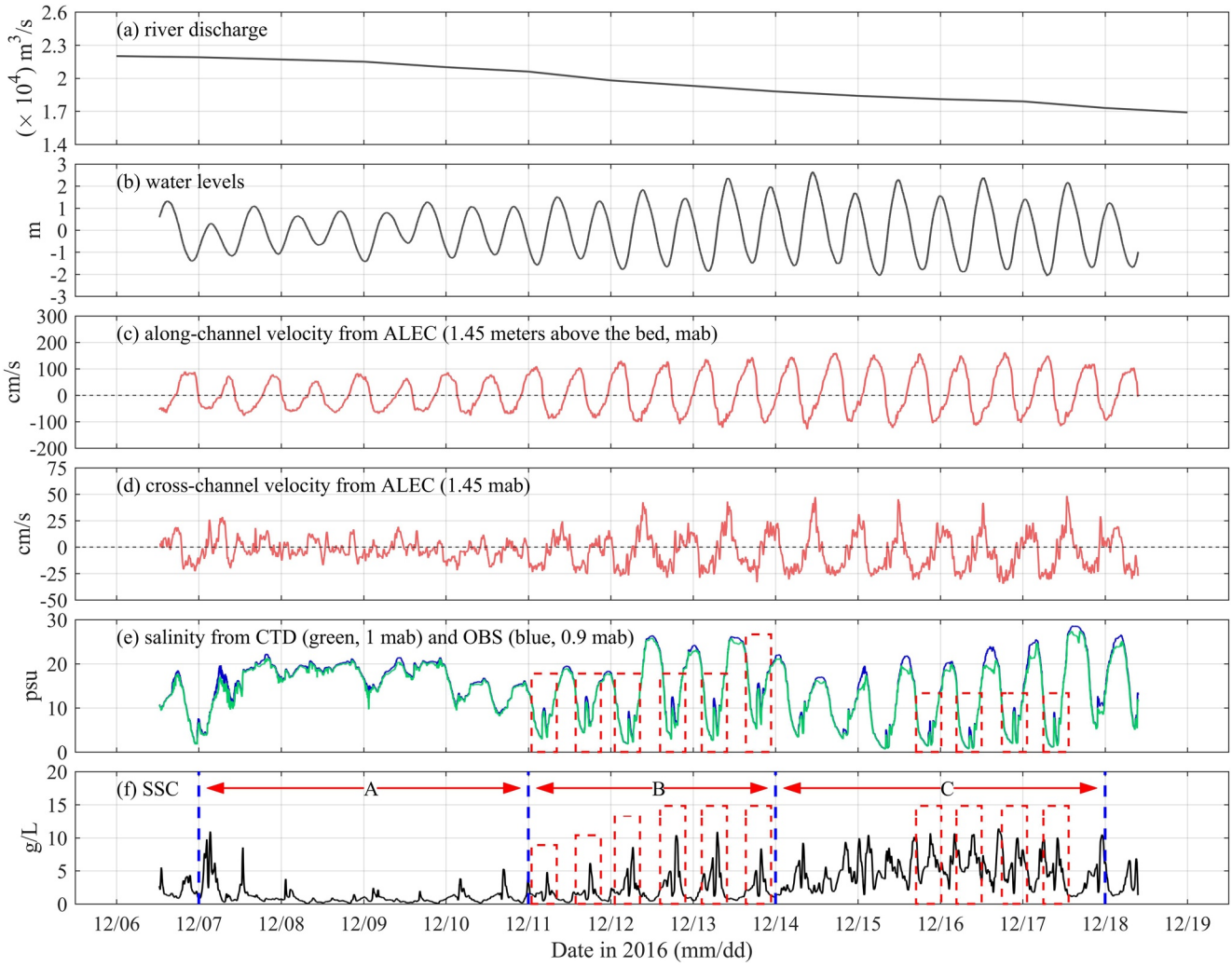

Figure 2. Time series of (a) river discharge, (b) water levels, (c) horizontal along-channel, and (d) cross-channel velocity monitored with ALEC, (e) salinity from CTD and OBS, and (f) suspended sediment concentration from OBS (at 0.9 m above the bed). For the along-channel flow, the positive value indicates direction of about 120° from the north, for cross-channel flow, the positive value indicates direction of about 30° from the north. For other locations, ebb currents (downstream) are positive in along-channel direction, currents from south shoal to north shoal (normal to ebb currents) are positive in cross-channel direction. CTD, Conductivity, Temperature, and Pressure Recorder; OBS, Optical Backscattering Sensor.

River discharge during this period was decreasing from 2.3 to 1.7 × 10^4 m^3/s (Figure 2a). The relatively low river discharge in dry season indicates the dominance of tidal forcing. Tidal form factor (F) calculated with observed data at the measuring site is 0.247 ($F = \left(K_1 + O_1\right) / \left(M_2 + S_2\right)$, using amplitude of each constituent), indicating semidiurnal tides. The tidal range (based on the water depth measured by the OBS pressure sensor) increased from about 2 m at neap tide to about 4 m around spring tide (Figure 2b). During neap tide conditions, the along-channel bottom velocity peaked at −77 to 83 cm/s (Figure 2c, ebb currents positive), increasing to −129 to 160 cm/s during spring tide. Along-channel velocities showed clear tidal variation, indicating effects of groyne-induced eddies were very limited for longitudinal flows in the deep channel (otherwise there would be lots of irregular fluctuations in the along-channel velocity curve rather than such a clear tidal variation). The cross-channel velocity was similarly strengthened during spring tide (Figure 2d). However, the cross-channel flow also developed a residual flow component, with negative flows (south shoal to north shoal positive) lasting longer, especially in the period before spring tide (Phase B). The cross-channel velocities could be affected by groyne fields, as groynes have a retention effect of salinity during ebb tide. The retention effect could consequently form a density gradient between the north shoal and the main channel, resulting in a lateral flow pattern. This is explained in detail in Section 3.1. It should be

noted that this lateral flow/transport process is not directly affected by groyne-induced eddies as these eddies mainly exist within groyne fields (Ge et al., 2012; Uijttewaal et al., 2001). During neap tide the salinity was higher, suggesting more pronounced salinity intrusion (Figure 2e). Salinity data acquired by CTD and OBS showed good consistency, both depicting the intratidal salinity variation during low water slack (LWS, and HWS for high water slack). The intratidal salinity variation lasted for about 1.5 h with a 5-psu salinity oscillation (Zhou et al., 2019). After neap tides, SSC greatly increased with clear periodic peaks (Figure 2f). Six SSC peaks with a similar intratidal variation pattern occurred during Phase B, the averaged SSC was 2.1 g/L. During Phase C, the averaged SSC was 5.0 g/L, four times larger than that of Phase A (1.1 g/L).

The SSC variation during Phase B showed a clear bimodal structure (Figure 2f) which corresponded to the intratidal salinity variation (Figure 2e). For the intratidal salinity variation, salinity first increased and then decreased, forming a subpeak in the trough. The SSC showed an opposite variation, i.e., it first decreased and then increased, forming a bimodal structure in the main peak. The intratidal salinity variation results from lateral salinity transport (Zhou et al., 2019). The synchronous but exactly opposite variation of salinity and SSC indicates the formation of the bimodal structure of SSC is related to similar lateral transport process. The water mass transported during this process had high salinity but low SSC, leading to the opposite variation of salinity and SSC—this will be explained in Section 3.1.

2.3. Numerical Model: Model Description and Validation

A three-dimensional suspended sediment transport model has been developed using the Finite-Volume Community Ocean Model (FVCOM) for the Changjiang Estuary (CE-FVCOM). FVCOM is an unstructured-grid coastal ocean model. In horizontal directions, a triangle mesh is used; in the vertical, a terrain-following sigma coordinate system (20 equidistant sigma layers) is prescribed. In a previous study (Zhou et al., 2019), a hydrodynamic model with semi-implicit scheme was set up, which well captured the two-layer structure flows and the complex intratidal salinity variation in the North Passage. This application has been extended with a sediment module (FVCOM-SED, Ge et al., 2015; Wu et al., 2011).

The suspended load model satisfies an advection-diffusion equation (Chen et al., 2013)

$$\frac{\partial C_i}{\partial t}+\frac{\partial uC_i}{\partial x}+\frac{\partial vC_i}{\partial y}+\frac{\partial\left(w-w_i\right)C_i}{\partial z}=\frac{\partial}{\partial x}\left(A_h\frac{\partial C_i}{\partial x}\right)+\frac{\partial}{\partial y}\left(A_h\frac{\partial C_i}{\partial y}\right)+\frac{\partial}{\partial x}\left(K_h\frac{\partial C_i}{\partial z}\right) \tag{1}$$

where C_i is the concentration for sediment i; A_h, K_h represent the horizontal and vertical diffusion coefficients, respectively; w_i is the settling velocity for sediment i; u, v, and w are velocity components in x, y, and z directions.

At the bottom, the net sediment flux is the difference between deposition and erosion (Chen et al., 2003; Zheng et al., 2003):

$$-K_h\frac{\partial C_i}{\partial z}-w_iC_i=E_i-D_i,z=-H \tag{2}$$

where K_h is the vertical eddy viscosity; H is the depth. The erosion rate E_i is calculated as

$$E_i=\Delta tQ_i\left(1-P_b\right)F_{bi}\left(\frac{\tau_b}{\tau_{ci}}-1\right) \tag{3}$$

where Q_i denotes the erosive flux; P_b represents the bottom porosity; F_{bi} is the fraction of sediment i in the bottom; τ_b, τ_{ci} are the bottom shear stress and critical shear stress for erosion of sediment i.

This sediment model considers single fraction of sediment with median grain size (D_{50}) of 0.008 mm. Flocculation is not considered in this model, as salt flocculation may play a minor role in the Changjiang Estuary (Guo & He, 2011; Song et al., 2013). The model is initialized with 1 m of sediment in the bed, with a settling velocity of 0.5 mm/s. Hindered settling is modeled using:

$$w_{\text{set}}=w_0*scale \tag{4}$$

Table 1
Data Source and Model Settings

Data source	
Wind	ERA-Interim data European Centre for Medium-Range Weather Forecasts
River discharge	www.cjh.com.cn, 1.7–2.3 × 10^4 m^3/s (Figure 2a)
Tidal forcing	TPXO 8 (Egbert & Erofeeva, 2002)
Settings	
Discretization	Finite-volume, semi-implicit scheme
Grid resolution	Minimum: ~200 m in the North Passage
Vertical layer	20 equidistant sigma layers
Internal time step	10 s
Number of time steps used to ramp the model from the initial field	5,000
Vertical Prandtl number	0.4
Horizontal Prandtl number	1.0
Sponge layer at the open boundary	0.0003
Grain size	0.008 mm
Initial settling velocity	0.5 mm/s
Initial bed thickness	1 m
Initial bed porosity	0.5

where w_0 is initial settling velocity, *scale* is the reduction scale which is set to 0.3. This adjustment for settling velocity operates in the lower two layers when the SSC is larger than 2.5 g/L. On the river boundary, the sediment concentration of the river discharge is specified as 0.3 g/L.

Waves are computed using the Simulating WAves Nearshore model forced with ERA-Interim (European Reanalysis) data from the European Centre for Medium-Range Weather Forecasts. Detailed data source and parameter information are listed in Table 1.

The CE-FVCOM model has been validated against hydrodynamics in previous studies (Ge et al., 2014, 2015; Guo et al., 2018; Zhou et al., 2019). Compared to length of groynes (1–2 km) and groyne fields (~5 km), grid resolution (~200 m) is able to resolve detailed processes, e.g., groyne-induced eddies (Ge et al., 2012). Validation of flow velocity, flow direction, and salinity is given in Figures 3a–3c, respectively. The OBS-measured SSC is used to further validate simulated SSC. A correlation coefficient is computed to quantify the agreement between the model and the data

$$CC = \frac{\mathrm{cov}\left(X,Y\right)}{std\left(X\right)\cdot std\left(Y\right)} \tag{5}$$

$cov\left(X,Y\right)$ is the covariance of variables X and Y, $std(X)$ is the standard deviation of X. The correlation coefficients of bottom flow velocity, direction, salinity, and SSC are 0.88, 0.96, 0.90, and 0.55, respectively.

The correlation coefficient of SSC is lower than that of the hydrodynamic variables because near-bed sediment dynamics are governed by complex processes and uncertainties in the bed properties. Nevertheless, the main characteristics of SSC are captured by the model, such as the bimodal structure and the pronounced peak around LWS (Figure 3d). The bimodal structure of SSC corresponds to the intratidal salinity variation—see the green box in Figure 3c—which has been attributed to lateral flows in earlier work (Zhou et al., 2019).

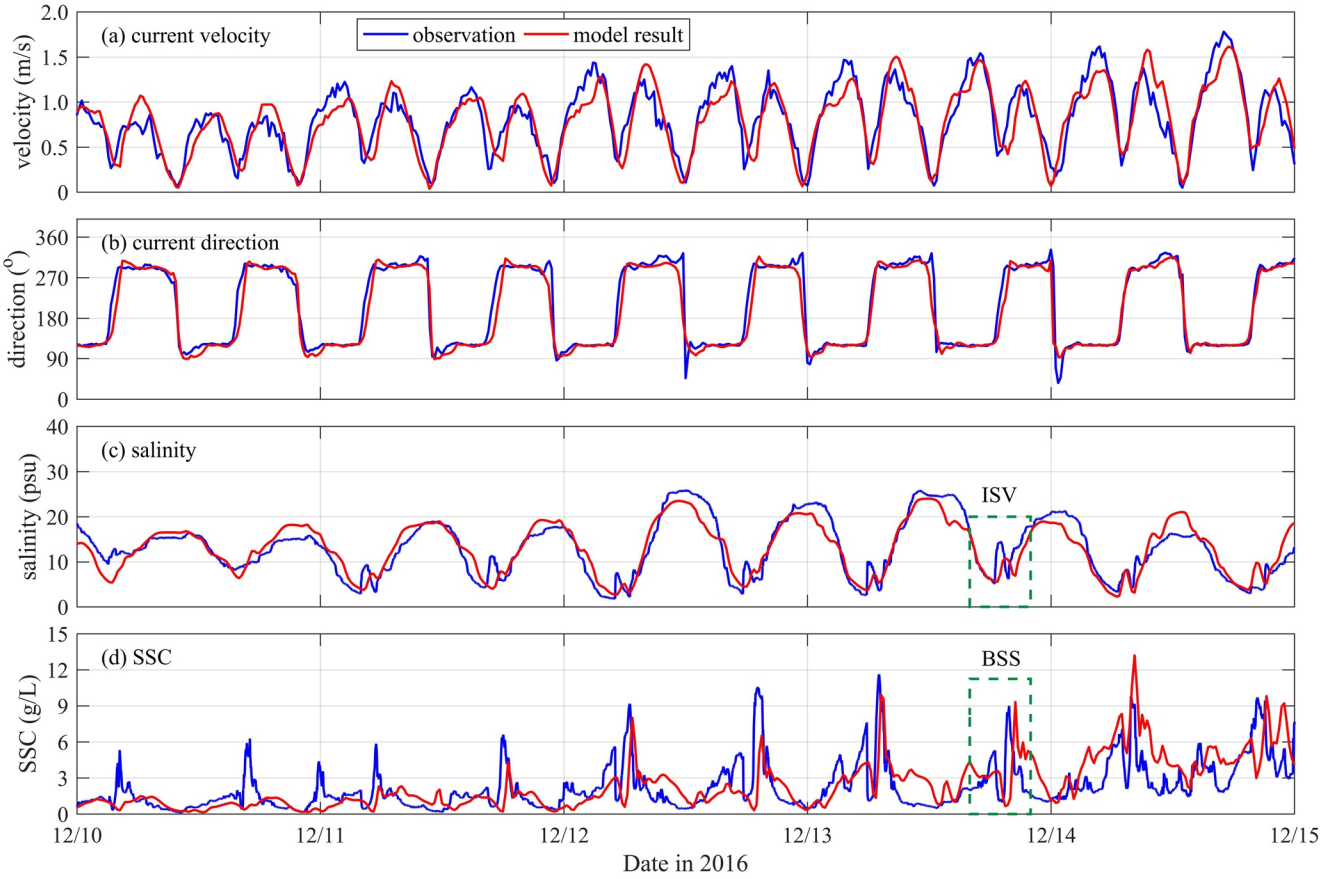

Figure 3. Model-data comparison between observed (blue) and simulated (red) results for near-bed current velocity (a), current direction (b), salinity (c), and suspended sediment concentration (d) at the measuring site. The green dashed boxes show a typical intratidal salinity variation and bimodal structure of SSC during LWS, which will be explained in more detail in Figure 4. "ISV" and "BSS" denote intratidal salinity variation and bimodal structure of SSC. SSC, suspended sediment concentration; LWS, low water slack.

3. Lateral Transport of Suspended Sediment

3.1. LWS: Low-Concentration Flows From North Shoal to Channel

The lateral transport during a bimodal-structure-of-SSC period (as identified in the previous section) is investigated in more detail using the numerical model. For this purpose, a typical bimodal structure of SSC observed and modeled on 12/13—see Figure 3d, was selected for detailed analysis. Figure 4 shows the near-bottom distribution of SSC during LWS. Near the end of ebb, bottom SSC in the main channel was higher as weak hydrodynamic conditions in the shoal area (marked with white box in Figure 4a) provided an environment for sediment to settle (Figure 4a). Meanwhile, due to the retention effect of groynes, a high-salinity water mass was trapped in the north groyne fields, forming a high-salinity and low-SSC condition on the north shoal. Instantaneous salinity and SSC of the observational site were 3.8 psu and 4.3 g/L. Mainly due to the density gradient, a shoal-to-channel bottom lateral flow was generated. The formation of this lateral flow has been introduced in detail in Zhou et al. (2019). This lateral flow transported saline but low-SSC water to the deep channel, leading to an increase in salinity and a decrease in SSC at the observational site (top-right panel in Figure 4b): the first stage of the intratidal salinity variation and bimodal structure of SSC. At 06:30, 2-g/L SSC contour went through the observational site (Figure 4c).

Near the bed, suspended sediment was mostly transported in the upstream direction due to flood currents. The high-concentration suspended sediment, in which the maximum SSC exceeded 10 g/L, was advected upstream, causing rapid increase of SSC at the observational site (Figure 4f). This implies that lateral flows were important for the decrease of SSC in the bimodal structure, the subsequent flood current governed the increase in SSC. The high suspended sediment concentration developed during LWS, due to sediment

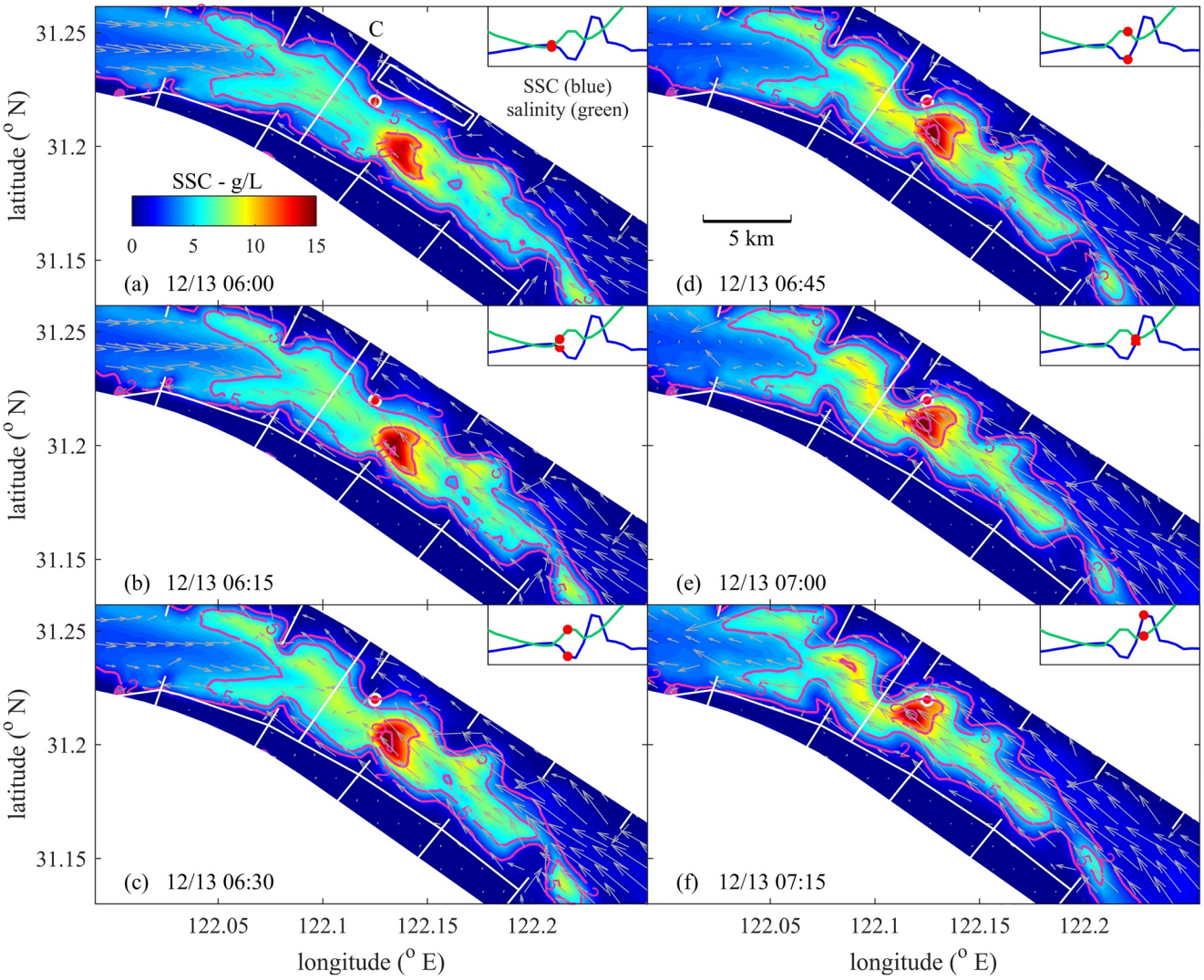

Figure 4. Spatial distributions of near-bed SSC at selected times (model result). The red dot indicates the observational site. The up-right inset shows the salinity (green) and SSC (blue); the red dot corresponds to the time of map plot corresponding to the inset. Arrows are near-bed velocities, indicating different stages in the bimodal-structure-of-SSC period. SSC contours of 2, 5, and 10 g/L are given with purple solid lines. The white rectangle in (a) indicates the north shoal area. SSC, suspended sediment concentration.

settling under weak hydrodynamics. This patch could be transported about 10 km upstream to the measuring site. During this process, increasing flow velocities gave rise to vertical mixing (Zhou et al., 2019), this high-concentration suspended sediment could spread to upper layer in the water column. It partly contributes to the ETM formation in the North Passage.

Although small amounts of suspended sediment were directly carried by the lateral flow from the north shoal, the lateral flow was still important for lateral transport of suspended sediment. This will be explored in more detail in Section 4.5 (Figure 12), together with the discussion about the impact of groynes. In the following section, we expand our analysis to the full tidal cycle in order to explain the origin and fate of the sediment patch.

3.2. HWS: Sediment Transport From Channel to South Shoal

During the ebb tide, SSC was highest in the deep channel, and was characterized by a band-like shape (Figure 5a). This high-SSC pattern was strengthened by strong ebb currents, developing into a broader

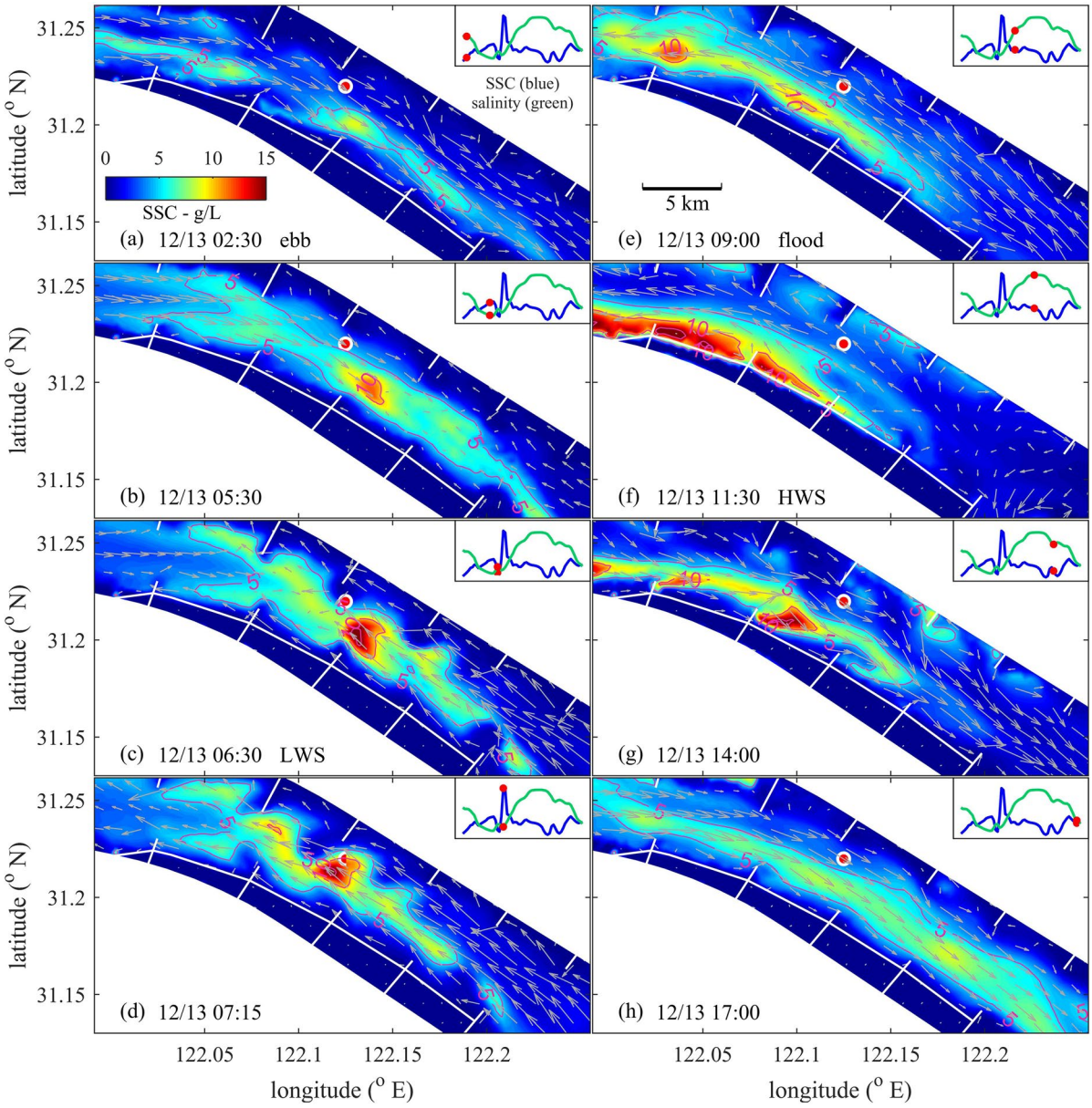

Figure 5. Spatial distributions of near-bed SSC in a complete tidal cycle (model result). The red dot indicates the observational site. The up-right inset shows variation of SSC and salinity. Arrows are near-bed velocities, indicating different stages in the tidal cycle. SSC contours of 5 and 10 g/L are given with purple solid lines. SSC, suspended sediment concentration.

high-turbidity band with higher concentration (Figure 5b). During LWS, the near-bed sediment concentration attained its maximum while at the same time the regular SSC shape deformed into a wave-like, patchy structure (Figures 5c and 5d). We attribute this deformation to the salinity-driven lateral flows described in Section 3.1. As these lateral flows originated from high-salinity waters trapped in the groyne fields, the wavelength of these SSC patches corresponded to the length of the groyne fields (about 5 km).

During the flood tide (Figures 5d–5f), the wave-like high SSC reverted to a longitudinal uniform patch, shaped by strong flood currents in the channel (Figure 5e). An important feature is that the high-turbidity band was transported to the south shoal (Figure 5f) during HWS. The southward transport mechanism is elaborated in detail in Section 4.3. This transport pattern can be integrated with lateral transport during LWS, attracting more attention to slack-water processes and dynamics. The high-concentration sediment was subsequently transported back to the main channel (Figure 5g) and continually transported seaward

(Figure 5h) by the ebb currents, forming the longitudinal tidal oscillation of the high-concentration suspended sediment in the North Passage.

In summary, during the observation period, two important processes took place, i.e., lateral transport of salt and sediment during LWS (Section 3.1) and sediment transport to the south shoal during HWS. These lateral exchange mechanisms are very important for the fate of the suspended sediments in the fairway, potentially contributing to net siltation rates.

4. Sediment Transport Mechanisms

In this section, by means of a sediment flux decomposition method and a momentum balance analysis, mechanisms for longitudinal and lateral transport of suspended sediment are investigated. In addition, effects of longitudinal sediment transport on sediment convergence in the channel, and effects of lateral sediment transport on deposition rate are also discussed.

4.1. Residual Sediment Flux

To explore the relative importance of various physical processes in more detail, the residual sediment flux per unit width is calculated and decomposed following (Dyer, 1988):

$$\begin{aligned}\frac{1}{T}\int_0^T\int_0^h ucdz_0 &= \frac{1}{T}\int_0^T\int_0^1 hucdzdt\\ &= \underbrace{h_0\overline{u_0}\,\overline{c_0}}_{T_1} + \underbrace{\langle\overline{u_t}\overline{h_t}\rangle\overline{c_0}}_{T_2} + \underbrace{\langle\overline{h_t}\overline{c_t}\rangle\overline{u_0}}_{T_3} + \underbrace{h_0\langle\overline{u_t}\,\overline{c_t}\rangle}_{T_4} + \underbrace{\langle\overline{h_t}\,\overline{u_t}\,\overline{c_t}\rangle}_{T_5} + \underbrace{h_0\overline{u_0'c_0'}}_{T_6} + \underbrace{h_0\overline{\langle u_t'c_t'\rangle}}_{T_7}\end{aligned} \tag{6}$$

where h is water depth; z is relative depth, $0 \le z \le 1$; u is current velocity; c is sediment concentration; T denotes period of tidal cycle; subscript "0" means tidally averaged whereas "t" means tidally fluctuating; overbars denote depth averages and quotation marks denote a depth-depending term; angled brackets denote tidal averages.

T_1 is the mean flow induced transport, i.e., transport due to Eulerian flow; T_2 is transport due to Stokes drift; together $T_1 + T_2$ represents advection transport. T_3, T_4, and T_5 are tidal pumping terms (Uncles et al., 1985a); T_6 is the transport resulting from vertical circulation which can be interpreted as salinity-driven estuarine circulation; T_7 is transport resulting from lag effects in settling and mixing.

This methodology was applied to decompose sediment fluxes in the North Passage in along-channel and cross-channel directions. Note that the flux calculated using this method is the vertical integrated flux at a specific location, making point results sensitive to a local variability in SSC and velocity. To avoid local variability, we used results of all locations along specific transects (B, C, and D) where the depth >10 m. With a typical channel depth of 12.5 m, the depth criterion of 10 m can provide a sufficiently large amount of locations representing deep channel dynamics. The sediment fluxes of the deep channel in both along-channel and cross-channel directions are shown in Figure 6. The jaggedness in Figure 6 is related to diurnal inequality in tidal forcing.

From transects B to D, the along-channel flux T_1 (related to processes that have longer timescales than the tide, e.g., the river discharge) was dominant (Figures 6a–6c). The magnitude of T_1 was maximal at spring tide (12/14–12/17) and decreased in the seaward direction (from transects B to D). Although the other advection term (T_2, Stokes drift) was directed landward, the total advection flux was seaward (Figures 6a–6c). Tidal pumping (terms T_3, T_4, and T_5) generated landward sediment transport in the upstream transects B and C, but was not large in the most seaward transect D. The seaward transport due to tidal pumping in section D was because of coupled asymmetry of stratification, sediment resuspension, and tidal currents (McSweeney et al., 2016). The water column was well mixed during the ebb tide and the stratification was enhanced from the end of LWS throughout the flood tide (Zhou et al., 2019). As a result, during the ebb tide, more sediment was transported compared to the flood tide due to stronger current velocities, more suspension (because of stronger near-bed velocities), and longer settling time (because of more pronounced vertical mixing). Therefore, asymmetric stratification and current velocities jointly generated an ebb-driven

Figure 6. Along-channel (left column) and cross-channel (right column) residual sediment flux per unit width of transects B (row 1), C (row 2), and D (row 3). For along-channel flux, positive value indicates seaward transport; for cross-channel flux, positive value indicates transport from the south shoal to the north shoal.

flux. In transect D, landward transport primarily resulted from vertical circulation (T_6). In transects B and C, tidal pumping and vertical circulation both contributed to landward sediment transport. Lag effects (T_7) constituted a minor contribution.

The combined effect of these mechanisms is seaward transport driven by advection in the upstream transect B and landward transport driven by tidal pumping and estuarine circulation in transects C and D (Table 2). This sediment convergence leads to deposition, which will be elaborated in more detail in Section 4.2.

In the main channel, the cross-channel flux was dominated by advection and vertical circulation in transects C and D (Figures 6e and 6f and Table 2), indicating the important role of lateral circulation in the deep channel. In transect B, T_7 was important (Figure 6d), indicating the role of lag effects in settling and mixing, that is, lag effects of suspended sediment responding to vertical velocity variation (Dyer, 1988). This different mechanism at transect B may be related to the channel curvature. The curvature radiuses of transects B and C are about 28 and 50 km, respectively, leading to a two times larger curvature-induced momentum term (and resulting in different lateral flow structures) at transects B than C (Zhou et al., 2019). For transects B and C (located in the channel bend), vertical circulation (T_6) resulted in a sediment flux toward the south shoal. Nevertheless, in transect D, T_6 was directed toward to the north. An important reason is position of transect D is close to the seaward limit of salt wedge during the ebb tide. Therefore, although the north groyne field also had a retention effect as the groyne field near the observational site, however, the density gradient between the north shoal and the main channel was small. The regular southward lateral

Table 2
Decomposed Sediment Flux Per Unit Width in Along-Channel and Cross-Channel Directions on Three Transects (Unit: kg/(m s))

	$T_1 + T_2$	$T_3 + T_4 + T_5$	T_6	T_7	Sum
B_{along}	8.81	−4.04	−1.92	0.43	3.28
C_{along}	4.40	−2.77	−3.13	0.44	−1.06
D_{along}	1.51	0.59	−2.33	−0.77	−1.00
B_{cross}	0.07	0.08	−0.17	−0.26	−0.27
C_{cross}	0.37	0.08	−0.48	0.03	0
D_{cross}	−0.64	−0.13	0.43	0.14	−0.21

Zero value in this table is because of approximation.

flow did not occur in transect D. Advection balanced the vertical circulation in transect C, whereas it exceeded the vertical circulation term in transect D. Combined, transport was directed southward in transects B and D, but negligible at transect C.

4.2. Sediment Accumulation in the North Passage

In this section, we further estimate the sediment accumulation in the North Passage resulting from longitudinal transport. The cumulative sediment transport (unit: kg) through a transect is calculated as

$$T = \sum_{t_0}^{t} c \cdot vel_n \cdot b \cdot d \tag{7}$$

where vel_n represents the cross-transect velocity; b, c, and d are width, SSC, and height of each computational cell; t_0 and t denote the start and end time of the calculation. Here, we define velocity in the ebb current direction as positive, thus mass increasing of sediment (unit: kg) of an area enclosed by transect P (landward) and Q (seaward) can be estimated as

$$M = T_P - T_Q \tag{8}$$

$M > 0$ indicates there is net sediment accumulation (mass increasing) in this area. The area between transects B and C (abbreviated as S_{BC}) is the curved area of the channel, where sediment was trapped during the whole observation period (Figure 7). Within in the 10-day period, the net sediment accumulation was about 3.3 million tons. S_{CD} is the straight part of the channel, which was losing sediment from 12/12 to 12/15, then recovering between 12/15 and 12/18. Overall, this area lost 0.8 million tons of sediment in the 10-day period (Figure 7). The whole section S_{BD} suffered from net sediment accumulation, mostly happened in the curved part of the channel.

The computed converging sediment mass can be compared to dredging data, to further evaluate the accuracy of the model. The density of dredged sediment is about 500–1,000 kg/m^3 (Fettweis et al., 2006), which means that in 10 days about 2.5–5 million m^3 accumulated. This corresponds to 91–182 million m^3/year when linearly extrapolated (assuming the dredging work aims at maintaining the depth of the channel). This is more than the dredging amount in 2016 between transects B and D (about 44 million m^3) but provides a reasonable order of magnitude, which is also a validation of this model. The overestimation may be the result of storm conditions (Hu et al., 2009; Nowacki & Ganju, 2018) occurring during the modeled period, with a strong north wind from 12/13 onwards leading to a maximum (observed) significant wave height exceeding 0.8 m. Strong wind and its induced wave height are important for sediment resuspension and transport outside the channel, which is subsequently transported back into the channel. Additionally, a short modeled period (as in our case) insufficiently accounts for feedback mechanisms between the flow and the bed: when deposition rates are too large the flow velocities become larger, and less sediment deposits. More sediment accumulation in the curved part (between transects B and C) compared to the straight part (between transects C and D) indicates different influence of groynes in the curved or straight part of the channel, requiring more research on the groyne layout. Here, we do not compare sediment accumulation to bed level changes from bathymetry surveys, because (1) we lack in situ observation of intratidal bed level changes, (2) bathymetry surveys cannot reflect actual sediment accumulation as the frequency of dredging work (daily to monthly) is higher than frequency of bathymetry surveys (seasonally to yearly).

4.3. Slack-Water Dynamics

Model results presented in Section 3.2 revealed a clear pattern of sediment transport to the south shoal during HWS, particularly around the curved part of the channel. Here, we further analyze the driving

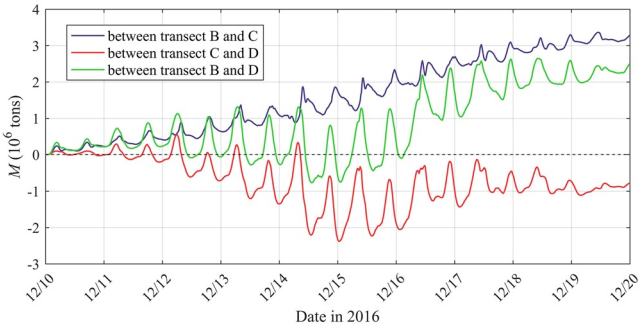

Figure 7. Sediment mass accumulated in the three areas enclosed by transects B, C (blue line), transects C, D (red line), and transects B, D (green line).

mechanisms for this channel-to-shoal transport through a momentum balance analysis. The governing equation for the lateral flow is

$$\underbrace{\frac{\partial v}{\partial t}}_{A}+\underbrace{u\frac{\partial v}{\partial x}+v\frac{\partial v}{\partial y}}_{B}+\underbrace{w\frac{\partial v}{\partial z}+fu}_{C}=\underbrace{-\frac{1}{\rho}\frac{\partial\left(P_H+P_a\right)}{\partial y}}_{D}+\underbrace{\frac{\partial}{\partial z}\left(K_m\frac{\partial v}{\partial z}\right)}_{E}+\underbrace{F_y}_{F} \quad (9)$$

where x, y, and z represent along-channel, cross-channel, and vertical directions in the Cartesian coordinate; u, v, and w are components in x, y, and z axes, respectively; ρ is density; P_H is hydrostatic pressure; P_a is the air pressure; f is the Coriolis parameter; and K_m is vertical eddy viscosity coefficient and F_y represent the horizontal momentum diffusion terms in y direction. The hydrostatic pressure P_H satisfies

$$\frac{\partial P_H}{\partial z}=-\rho g \Rightarrow P_H=\rho_0 g\zeta+g\int_z^0\rho dz \quad (10)$$

where g is the gravitational acceleration. In Equation 9, A–F are local acceleration, advection, Coriolis force, pressure gradient, vertical diffusion, and horizontal diffusion. The Coriolis force and pressure gradient terms on transect B are shown in Figure 8, with positive values indicating flows from the deep channel to the north shoal. The density effect of sediment was not included in this model, neither in this momentum balance analysis.

To unravel driving forces for southward sediment transport during HWS and its movement back to the main channel during the early ebb tide, we select three typical moments for analysis (first column in Figure 8).

During the early stage of flood tide (Figure 8a), the Coriolis force term (with a magnitude of 4–6 $\times 10^{-5}$ m/s^2 in the main channel) was toward the north shoal on transect B (marked with red line in Figure 8a). The total pressure gradient force was weaker in the channel, with a value of $-1 \sim -4 \times 10^{-5}$ m/s^2. At this moment, as the flood current had not affected transect B, the salinity (also density) was laterally uniform, and therefore the baroclinic pressure gradient was weak (Figure 8c). The barotropic pressure gradient was the main contributor (Figure 8d), because the flood currents deflected to the north shoal and raised the water level on the north side.

Later in the flood tide (Figure 8e), the total pressure gradient force reached -3×10^{-4} m/s^2 in the deep channel, while the Coriolis force was about 1–2 $\times 10^{-4}$ m/s^2. The difference between these two terms was around 10^{-4} m/s^2, which is able to generate a lateral flow in this channel (Zhou et al., 2019). This explains the sediment transport to the south shoal during HWS. Moreover, the combined baroclinic and barotropic pressure gradient terms contributed equally to the strong momentum toward the south (Figures 8g and 8h).

During the early stage of ebb tide (Figure 8i), a high-SSC water patch on the south shoal started to move back to the main channel, driven by a high positive pressure gradient on the south shoal (about 3 $\times 10^{-4}$ m/s^2). Furthermore, the baroclinic pressure gradient was the main contributor to the pressure gradient term (Figure 8k) as the salt had been transported to the south and the density effect of salinity was more important than the lateral difference of water level.

To demonstrate the importance of the baroclinic pressure gradient (i.e., the salinity-induced density effect), we simulated a barotropic scenario in which salinity of sea water was set to zero. Model results shows the distribution of bottom SSC (Figure 9a) did not have the same wave-like, patchy structure found in the original case (Figure 9c), supporting our earlier conclusion (in Section 3.2) that the wave-like structure resulted from salinity-driven density currents. More importantly, the sediment transport to the south shoal during HWS also weakened (Figure 9b) compared to the original case (Figure 9d). This difference resulted from the baroclinic pressure gradient. However, the distribution of bottom SSC still showed a weak southward deflection (Figure 9b) because of the channel curvature and configuration of groynes.

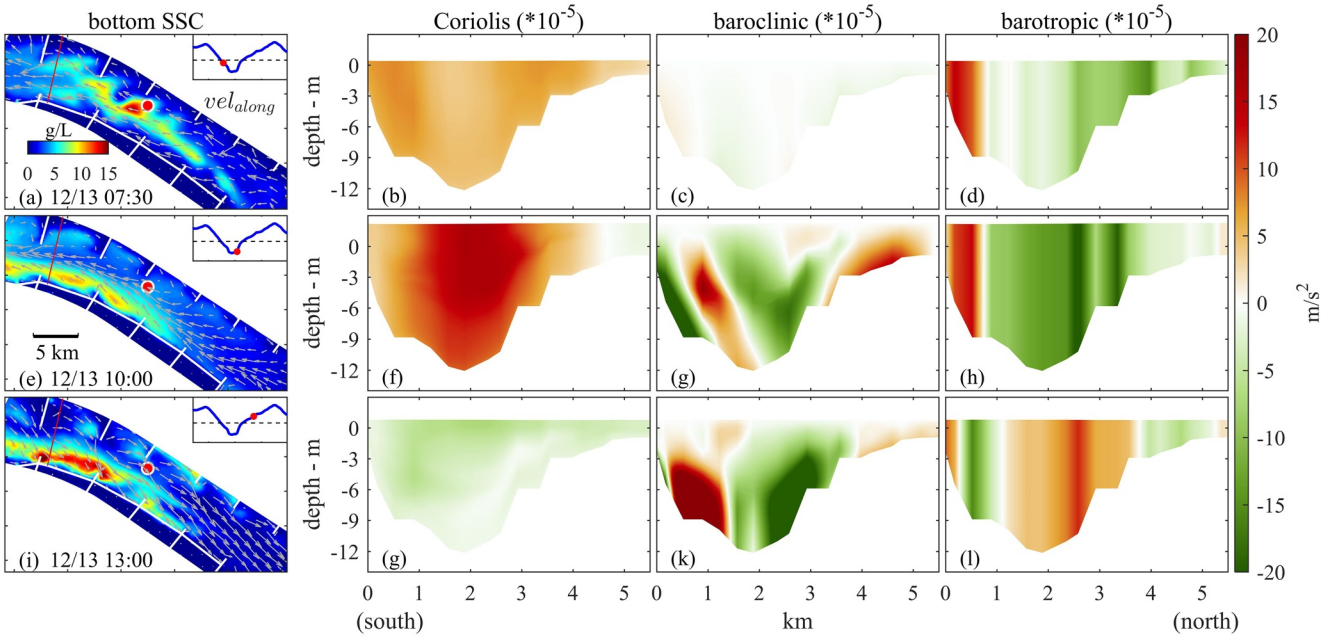

Figure 8. Momentum balance analysis of transect B (Figure 1). Coriolis term (b, f, and g), baroclinic pressure gradient term (c, g, and k), and barotropic pressure gradient term (d, h, and l) of early stage of flood tide (a), late stage of flood tide (b), and early stage of ebb tide (c). The red line represents transect B and the red dot is the observational site. The up-right inset shows along-channel velocity to indicate stage in a tidal cycle, positive values denote downstream (ebb) currents.

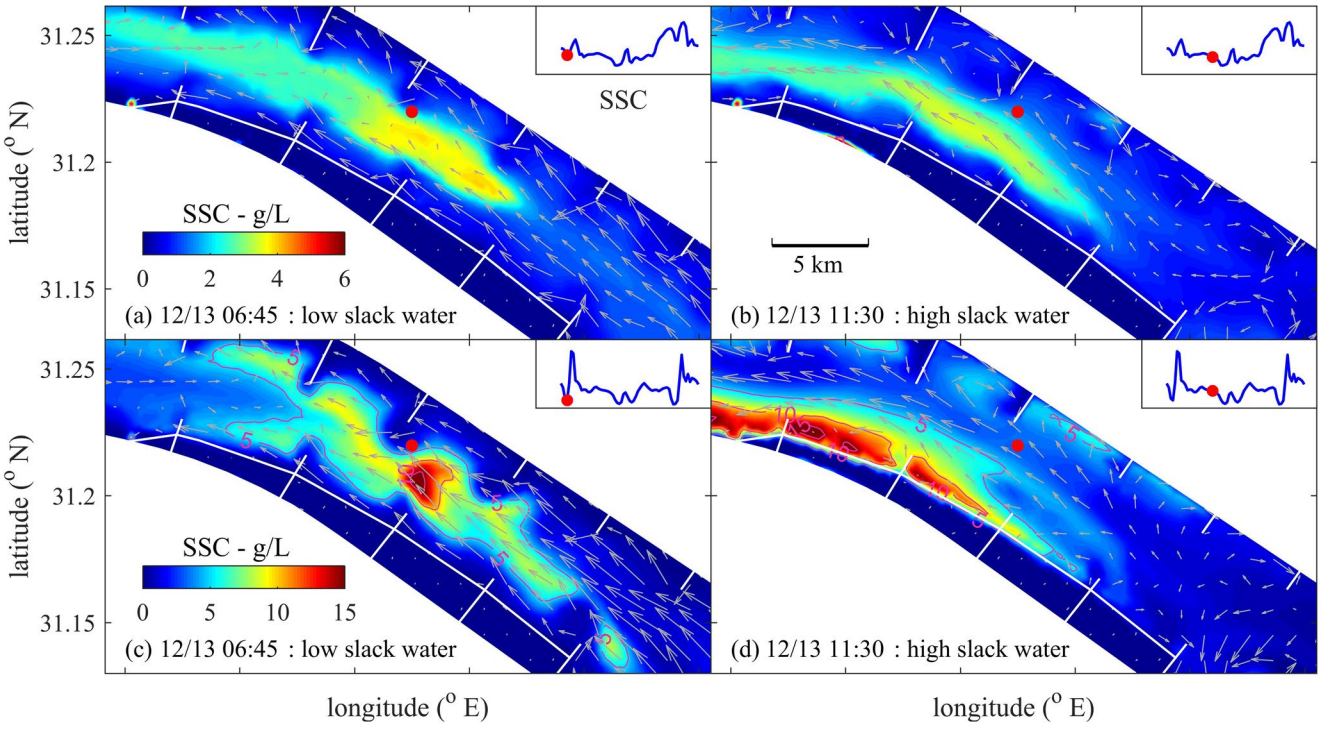

Figure 9. A comparison between a barotropic scenario (a and b) and the original (baroclinic) scenario (c, d, same with results in Figures 4 and 5). Spatial distributions of near-bed SSC and flow velocity during LWS (a), (c) and HWS (b), (d) in the new nonsalinity scenario (a and b) and the original scenario (c and d). Arrows are near-bed velocities, indicating different stages in the tidal cycle. SSC contours of 5 and 10 g/L are given with purple solid lines. The red dot is the observational site. SSC, suspended sediment concentration; LWS, low water slack.

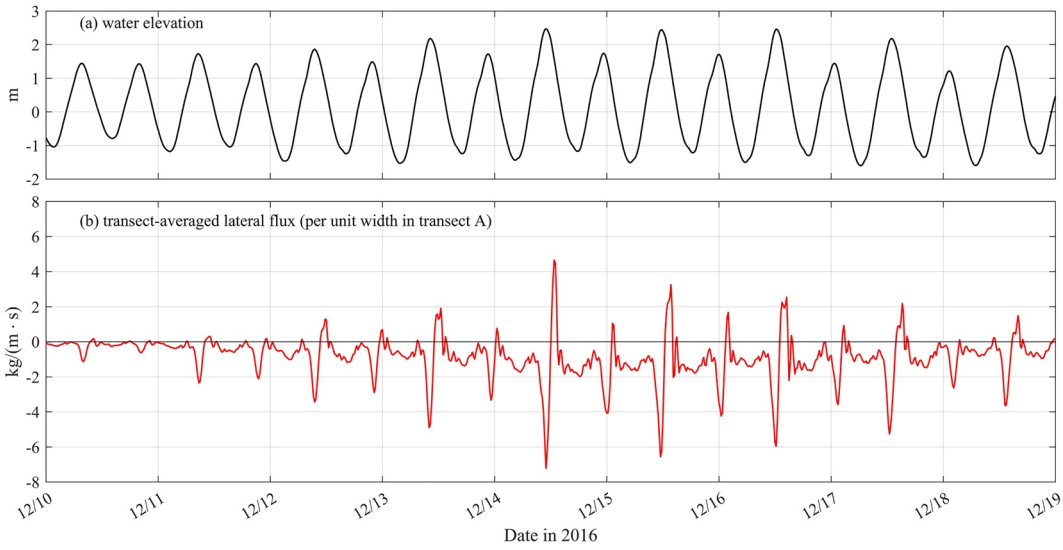

Figure 10. Water elevation (a) at a site (122.0945°E, 31.2082°N) in transect A (the along-channel transect that encloses two groyne fields on the south shoal in Figure 1) and transect-averaged lateral transport flux of suspended sediment in transect A (b), positive value indicates transport from the south shoal to the north shoal.

Because transect B is in the channel bend, curvature-induced momentum (defined as $\frac{u_s^2}{R}$ in a curvilinear coordinate system) could be important. Here, u_s is the longitudinal velocity magnitude and R is the radius of curvature. For transect B, R is about 28.7 km in the deep channel. The maximum flood current velocity was about 1.6 m/s at the bottom and 2.2 m/s at the surface. This term was about 8.9×10^{-5}–1.7×10^{-4} m/s^2 from the bottom to the surface during flood maximum, toward the north side of the channel. The vertical differences of this term could result in a clockwise (originating from the flood current) lateral circulation and enhance the southward transport of sediment in the bottom layer. This explains the weak southward deflection in Figure 9b.

The curvature-induced centrifugal force was strongest during maximum flood and declined with the decrease of the flood current. During HWS, this term was small because of the weak current, however, its accumulated effect during the whole flood tide still contributed to the near-bed southward sediment transport. In summary, the southward sediment transport during HWS was mainly caused by the combined baroclinic and barotropic pressure gradient force. This southward lateral transport is further illustrated for transect A (Figure 10). The averaged lateral transport flux indicates an overall transport from the deep channel to the south shoal. For example, the averaged flux from 12/13 to 12/14 was about −0.82 kg/(m s). During this period, the maximum flux toward the south shoal was about −4.9 kg/(m s), which was about 2.6 times the maximum flux toward the deep channel (about 1.9 kg/(m s)). The maximum flux toward the south shoal all occurred during HWS (Figure 10), in agreement with our emphasis on southward transport of suspended sediment during this period. Subsequent effects of the southward transported suspended sediment are investigated in the following section.

4.4. Deposition During HWS

Computed bed level changes reveal that the channel eroded during peak flow conditions, whereas deposition prevailed during slack tide conditions (Figure 11). It also shows that deposition was persistent in the groyne fields (to the south as well as to the north). However, most striking is the accumulation rate of sediments on the south shoal during HWS (Figure 11b).

Pronounced southward lateral transport results from the barotropic and baroclinic pressure gradients (Section 4.3). In this section, we investigate deposition potential in more detail and discuss the effect of the southward sediment transport during HWS. Sediments are kept in suspension by turbulent motions, and

especially for sediments with a considerable settling velocity, absence of turbulence leads to rapid deposition of sediments. Even more, steep sediment concentration gradients suppress turbulent mixing, which leads to faster settling, in turn further decreasing turbulent mixing (Winterwerp, 2001, 2006). We therefore analyze the water column stability with a Bulk Richardson number. The bulk Richardson number R_{ib} is calculated as

$$R_{ib} = \frac{gD\Delta\rho}{\overline{\rho_w}\left|\vec{u_s}^2\right|} \tag{11}$$

where D represents water depth; $\Delta\rho$ denotes bottom-surface density difference; $\overline{\rho_w}$ is vertically averaged density; and $\vec{u_s}$ is surface current velocity. Figure 12 shows the result of $\log_{10}\left(R_{ib} / 0.25\right)$, positive values indicating stratifying conditions.

During peak flood flow, the whole water column was slightly stratified in the main channel (Figure 12a), whereas stronger stratification dominated over the north shoal. During HWS (when sediment was transported to the south shoal—see Figure 5f), the area with high deposition rates (Figure 11b) was highly stratified (Figure 12b), showing a high probability of enhanced sediment accumulation on the south shoal. During the ebb maximum, the main channel showed a well-mixed condition due to great surface current velocity (Figure 12c). During LWS, the main channel was dominated by strong stratification (Figure 12d), and the stratification showed a patched-like pattern, that is, stratification was stronger in the main channel and weaker in groyne fields.

Sediment was regularly transported southward during HWS (showed in Section 3.2 and explained in Section 4.3). Although during early ebb, part of the sediment would be transported back to the main channel, modeled bed level changes and water column stability still indicate the deposition potential and accumulation effect due to this transport pattern.

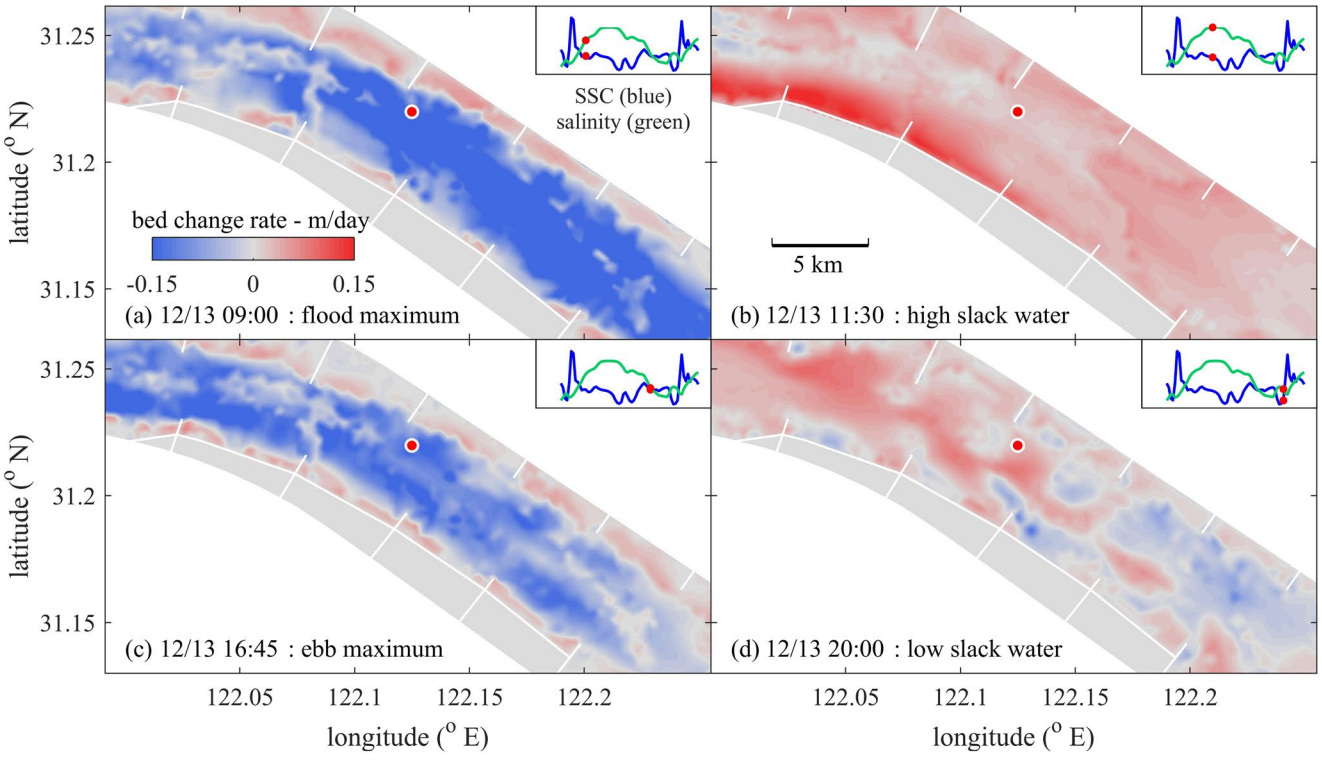

Figure 11. Distribution of bed level change rate (m/day) in the channel. Positive values (red) indicate deposition. The up-right inset shows variation of SSC and salinity. SSC, suspended sediment concentration.

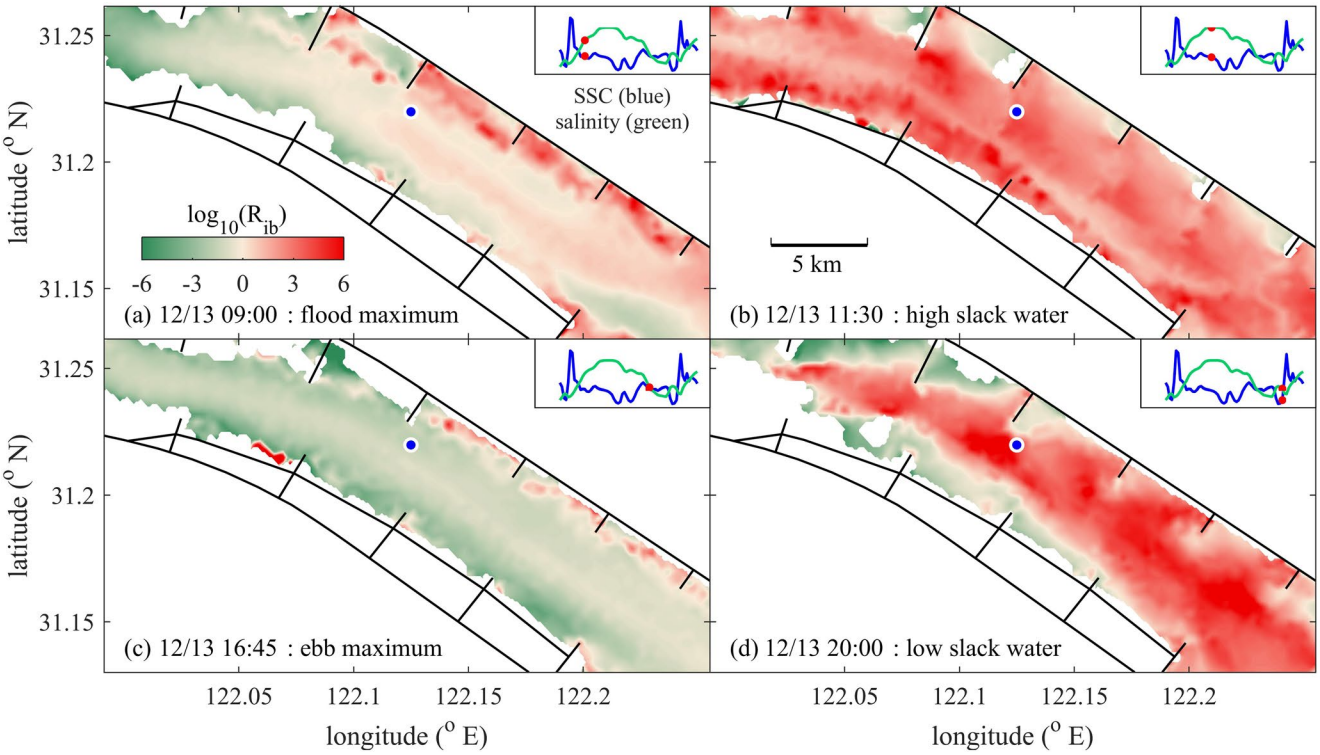

Figure 12. Distribution of bulk Richardson number ($\log_{10}(R_{ib} / 0.25)$) in the channel. The up-right inset shows variation of SSC and salinity. The blue dot is the observational site. The blank area is because of negative R_{ib} when converted to a logarithm. SSC, suspended sediment concentration.

4.5. Effect of Groyne Removal

The decomposed residual transport terms (Section 4.1) illustrated the importance of lateral circulation (term T_6 in Figures 6d–6f) to lateral transport of suspended sediment, especially at transect C. Transect C is close to a north groyne and is heavily affected by the regular lateral flow during LWS. To demonstrate the influence of groynes, the nearest groyne to the observational site was removed in the model. Earlier work (Figure 14 in Zhou et al. (2019)) showed that such removal strongly reduced lateral flow during LWS. By keeping or removing the nearest groyne, we therefore have two cases with (Case 0) or without (Case 1) lateral flow during LWS, which can be used to quantify the effect of this groyne-induced impacts on lateral flow and sediment transport. Removing all groynes would greatly influence the overall flow patterns, leading to substantial change in longitudinal processes, and these longitudinal changes also influence lateral flows and sediment transport. However, removing one single groyne helps to keep the overall flow field and allows detailed analysis of effects of groynes on lateral processes. Besides, since the retention effect of groynes on salinity is not obvious on the south side (Figure 13a), the south groyne removed case is not conducted in this study. The removed groyne is about 1.52 km, and it is connected with eight grid cells. This grid resolution is enough to resolve effects of this groyne.

In this section, near-bottom residual sediment flux at the observational site is calculated for Case 0 and Case 1 to explore effect of this lateral flow on sediment transport pattern, following (Uncles et al., 1985b):

$$\langle u \cdot c \rangle = u_0 c_0 + \langle u_t c_t \rangle \tag{12}$$

where definition of bracket, subscript "0" and "t" are the same with that defined in Equation 6. $u_0 c_0$ denotes the advection transport due to residual flow, $\langle u_t c_t \rangle$ is transport due to tidal pumping.

In the along-channel direction, advective transport becomes weaker when the groyne is removed (Case 1) although transport patterns for these two cases is similar (Figure 13c). This is because the groyne has the effect of regulating flows, which could enhance current velocity and benefit advective transport. However,

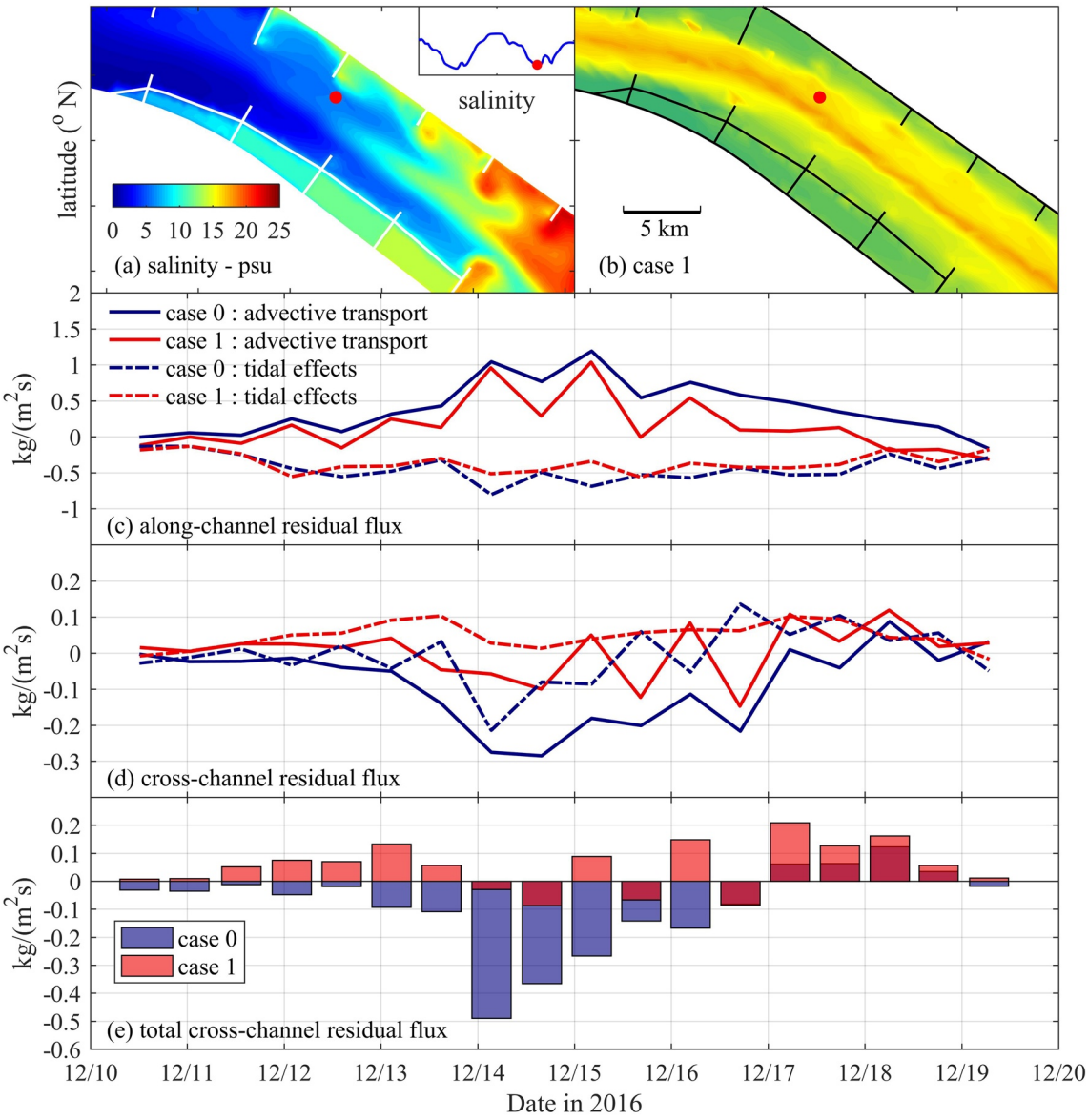

Figure 13. Numerical cases setting and single-point residual sediment flux, Case 0: standard case with near-bed salinity distribution during low water slack (a); Case 1: the groyne nearest to the observational site is removed, marked with white rectangle (b); decompositions of residual flux at the observational site in along-channel (c) and cross-channel (d) direction; and difference of cross-channel residual flux between Case 0 and Case 1 (e). The positive value in (c) indicates direction of about 120° from the north, the positive value in (d) indicates direction of about 30° from the north.

as only one groyne is removed in Case 1, the impact of this adjustment is relatively local, and will not cause substantial difference to the overall flow field, especially to the longitudinal currents, supporting the reason for removing one single groyne. Differences of tidal effects term between Case 0 and Case 1 are also not important for the same reason. The influence of only one single groyne becomes important, however, in the cross-sectional direction (Figure 13d). Values of the advective transport term increases for Case 1, indicating a decrease of north-shoal-to-channel residual transport. For Case 0, the advective transport is negative for the most time; while in Case 1, half of tidal cycles have a positive advective term, that is, an opposite flux (channel-to-shoal). This effect is also observed in the tide-induced transport term (Figure 13d), which is significantly increased by the adjustment of the groyne. With one groyne removed, the tide-induced transport is positive for most of the period, indicating a continuous channel-to-shoal residual transport. Removing one groyne could reduce effects of groynes on narrowing the channel and strengthening currents, leading to tidal flow easier to flush into the groyne field. The net effect of this groyne adjustment on total cross-chan-

nel residual flux ($\langle u \cdot c \rangle$) is shown in Figure 13e. After the nearest groyne is removed, the north-shoal-to-channel residual transport decreases, and in some tidal cycles, the residual transport even changes in direction. This result shows effects of groynes on lateral transport of suspended sediment and these effects include the lateral flow during LWS and the consequent effect on lateral sediment transport.

The lateral flow develops close to the north groynes and seems to be site specific. However, this process is important near every north groyne in the straight part of the channel, and therefore the total effect is significant. On the other hand, the lateral flow during LWS is caused by salinity retention in the groyne fields, and this retention effect is determined by groyne dimensions, including the length, height of groynes, and distance between them. In this study, the retention effect is observed in the north part of the channel. However, we believe it can also occur near south groynes if their length is increased. Moreover, the radius of the channel is also important for the asymmetric features between north and south shoals. These hypotheses will be investigated in future studies.

5. Discussion

Numerous studies about siltation issues have been conducted, focusing on (1) mechanisms for longitudinal convergence of sediment, including ETM dynamics (Burchard et al., 2018); (2) lateral circulation and consequently induced sediment trapping (Chen et al., 2020; Yang et al., 2014); (3) vertical processes in sediment dynamics, including settling and resuspension (Dankers & Winterwerp, 2007; Ge et al., 2018). This research provides some new information about sediment transport, which is important to deposition issues in a highly silted channel-shoal system. We report and stress the importance of lateral transport of suspended sediment during HWS and LWS (Section 3) in the North Passage, and explain the driving mechanism (Section 4.3) and deposition potential (Section 4.4) of sediment transport during HWS. For LWS conditions, we explain the formation of bimodal structure of SSC (Section 3.1) and demonstrate the effect of this lateral transport on residual flux (Section 4.5). Except for slack-water dynamics, knowledge about impact of groynes is also extended. The presence of groynes significantly affects lateral flows, distribution of high-concentration suspended sediment, and lateral transport patterns (Sections 3.1 and 4.5). Removing one groyne can reduce the lateral flow and sediment transport flux at the observational site during LWS. However, removing multiple groynes may change the overall flow dynamics in the North Passage and South Passage, and therefore determining the overall effect of groynes on transport requires additional research.

Lateral transport of suspended sediment and mass exchange have been studied extensively as part of earlier work. Geyer et al. (1998) unraveled a channel-to-shoal transport mechanism related to lateral salinity gradient caused by differential advection of the longitudinal salinity gradient. Additionally, Huijts et al. (2006) applied a two-dimensional idealized model and emphasized the importance of lateral density gradients which usually induce more sediment transport than Coriolis force in estuaries. The present study further supports the importance of lateral salinity gradient to sediment transport, and particularly focuses on lateral salinity gradient during high and low water slack. Zhou et al. (2019) reported a salinity-induced density gradient and the lateral flow thereon due to retention of high-salinity water by groynes. This companion study further investigated the lateral sediment transport due to this lateral flow during LWS, and also expanded findings to lateral process during HWS, extending our understanding of slack-water dynamics. Slack-water dynamics are important because the weak hydrodynamics during slack-water conditions are suitable for sediment settling and deposition, which can greatly influence channel morphology. Bed level change rate demonstrates that large amount of sediment deposition could occur on shoals during high and low water slack. Therefore, findings presented here provide important insights into siltation issues in channel-shoal systems.

Groynes are most commonly used in low-land rivers and coastal zones, but they are also used in estuaries, e.g., the Changjiang Estuary, the Ems Estuary (van Maren et al., 2015), and the Weser Estuary (Hesse et al., 2019). These systems are all confronting severe siltation. However, in none of these areas the role of groynes in relation to lateral exchange mechanisms has been thoroughly investigated. Groynes are designed to accelerate the flow in navigation channels, thereby reducing channel siltation. The work presented here suggests that the role of groynes is much more complex in stratified estuarine environments, as (1) salinity gradients can complicate the effect of groynes and (2) existence of groynes can affect salinity gradients.

Therefore, their design in estuarine environments may need to be revisited. Although our findings indicate a groyne-induced mechanism that can enhance the lateral transport of suspended sediment from the north shoal to the main channel, it is only one of the potential effects of groynes. Other effects are also important and may have opposite influences on sediment transport. For application and evaluation of groynes in estuaries, more studies are needed.

The current model only includes single fraction of sediment which may affect the accuracy of reflecting sediment dynamics, as sediment properties are important in many aspects, for instance, settling and resuspension, critical shear stress for erosion, and so on. This study is also limited by lack of some physical processes in the model. The current model can well simulate the suspension, transport, and deposition of sediment. However, it is not able to simulate processes like slope-induced slide of fluid mud or bed layer from the shallow shoal to the deep channel, which may be crucial to sediment redistribution in a channel-shoal system and determine the dredging demand in the navigational channel. Another note of caution is due here since density effects caused by sediment concentration are not included in the model, salinity plays the most important role in lateral processes. Even though main characteristics of salinity and SSC variation are captured, the model can be improved by including sediment-caused density effects. These aspects should be improved as part of our future work.

6. Conclusions

By means of in situ observations and a validated high-resolution unstructured-grid sediment transport model, this paper studies the lateral transport of suspended sediment in a tidal channel-shoal system. The model also demonstrates the effect of groynes on hydrodynamics and sediment dynamics.

The model results showed that high-concentration suspended sediment layer with the maximum SSC exceeding 10 g/L occurred in the channel. In the longitudinal direction, the ETM resulted from convergence of sediment by river flow on one hand, and a combination of tidal pumping and estuarine circulation (both equally important) on the other hand. During the late stage of flood tide, the high-concentration suspended sediment layer moved from the channel toward the south shoal, resulting in highly stratified conditions on the south shoal. A momentum balance analysis revealed that this southward flow and sediment transport was primarily driven by the pressure gradient force. Sediment was deposited on the south shoal because of strongly stratified conditions, leading to suppression of turbulent mixing. During LWS, the existence of groynes triggered a north-shoal-to-channel lateral flow. These sediment transport mechanisms operating during HWS and LWS highlight the importance of slack-water dynamics when addressing on siltation issues in channel-shoal systems. River discharge was in the range of $1.7–2.4 \times 10^4$ m^3/s (continuously decreasing during the study period), the effects of this fluvial component were limited during the dry season. However, the fluvial component can greatly impact tidal dynamics and riverine sediment supply in the wet season.

Our results also showed that groynes are important for lateral sediment transport in this system. Groynes can show retention effects on salinity during the ebb tide. By affecting the flow field and the salinity distribution, groynes can lead to a shoal-to-channel lateral flow and enhance lateral sediment transport, impacting the sediment redistribution in the cross-channel direction. This mechanism plays a role in 4–5 groyne fields on the north side of the North Passage. Findings in this study indicate a new mechanism for groyne-induced enhancement of lateral transport of suspended sediment from the north shoal to the main channel. Groynes are widely used all over the world for preventing siltation rates in navigation channels (riverine most). Yet, the impact of groynes on hydrodynamics and sediment issues, especially in estuarine environments where salinity gradient is widespread, still need to be further investigated.

Data Availability Statement

All data sets used in this study are publicly available at https://figshare.com/s/1508cdc878aade130b7c.

Acknowledgments
This research was supported by the National Natural Science Foundation of China (Grant 41776104), the National Key R&D Program of China (Grant 2016YFA0600903), KNAW Project (Grant PSA-SA-E−02), Science and Technology Commission of Shanghai Municipality (18DZ1206401), and the Fundamental Research Funds for Central Public Welfare Research Institutes (CKSF2019411/HL).

References

Burchard, H., Schuttelaars, H. M., & Ralston, D. K. (2018). Sediment trapping in estuaries. *Annual Review of Marine Science*, *10*(1), 371–395. https://doi.org/10.1146/annurev-marine-010816-060535

Chen, C., Beardsley, R., Cowles, G., Qi, J., Lai, Z., Gao, G., et al. (2013). *An unstructured grid, finite-volume coastal ocean model (FVCOM)—User Manual*. (Tech. Rep., SMAST/UMASSD-13-0701. New Bedford: School of Marine Science and Technology, University of Massachusetts Dartmouth. https://doi.org/10.1017/CBO9781107415324.004

Chen, C., Liu, H., & Beardsley, R. C. (2003). An unstructured grid, finite-volume, three-dimensional, primitive equations ocean model: Application to coastal ocean and estuaries. *Journal of Atmospheric and Oceanic Technology*, *20*(1), 159–186. https://doi.org/10.1175/1520-0426(2003)020<0159:AUGFVT>2.0.CO;2

Chen, L., Gong, W., Zhang, H., Zhu, L., & Cheng, W. (2020). Lateral circulation and associated sediment transport in a convergent estuary. *Journal of Geophysical Research: Oceans*, *125*, e2019JC015926. https://doi.org/10.1029/2019JC015926

Chen, S. N., Sanford, L. P., & Ralston, D. K. (2009). Lateral circulation and sediment transport driven by axial winds in an idealized, partially mixed estuary. *Journal of Geophysical Research*, *114*, C12006. https://doi.org/10.1029/2008JC005014

Chen, W., & de Swart, H. E. (2018). Longitudinal variation in lateral trapping of fine sediment in tidal estuaries: Observations and a 3D exploratory model. *Ocean Dynamics*, *68*(3), 309–326. https://doi.org/10.1007/s10236-018-1134-z

Dankers, P. J. T., & Winterwerp, J. C. (2007). Hindered settling of mud flocs: Theory and validation. *Continental Shelf Research*, *27*(14), 1893–1907. https://doi.org/10.1016/j.csr.2007.03.005

de Nijs, M. A. J., & Pietrzak, J. D. (2012). Saltwater intrusion and ETM dynamics in a tidally-energetic stratified estuary. *Ocean Modelling*, *49*(50), 60–85. https://doi.org/10.1016/j.ocemod.2012.03.004

Dronkers, J. (1996). The influence of buoyancy on transverse circulation and on estuarine dynamics. In D. G. Aubrey, & C. Friedrichs (Eds.), *Buoyancy effects on coastal and estuarine dynamics* (pp. 341–356). Washington, DC: American Geophysical Union. https://doi.org/10.1029/CE053p0341

Dyer, K. R. (1988). Fine sediment particle transport in estuaries. In *Physical processes in estuaries* (pp. 295–310). Berlin, Heidelberg: Springer. https://doi.org/10.1007/978-3-642-73691-9_16

Egbert, G. D., & Erofeeva, S. Y. (2002). Efficient inverse modeling of barotropic ocean tides. *Journal of Atmospheric and Oceanic Technology*, *19*(2), 183–204. https://doi.org/10.1175/1520-0426(2002)019<0183:EIMOBO>2.0.CO;2

Fettweis, M., Francken, F., Pison, V., & Van den Eynde, D. (2006). Suspended particulate matter dynamics and aggregate sizes in a high turbidity area. *Marine Geology*, *235*(1–4), 63–74. https://doi.org/10.1016/j.margeo.2006.10.005

Ge, J., Chen, C., Qi, J., Ding, P., & Beardsley, R. C. (2012). A dike–groyne algorithm in a terrain-following coordinate ocean model (FVCOM): Development, validation and application. *Ocean Modelling*, *47*, 26–40. https://doi.org/10.1016/j.ocemod.2012.01.006

Ge, J., Ding, P., & Chen, C. (2014). Low-salinity plume detachment under non-uniform summer wind off the Changjiang Estuary. *Estuarine, Coastal and Shelf Science*, *156*(1), 61–70. https://doi.org/10.1016/j.ecss.2014.10.012

Ge, J., Shen, F., Guo, W., Chen, C., & Ding, P. (2015). Estimation of critical shear stress for erosion in the Changjiang Estuary: A synergy research of observation, GOCI sensing and modeling. *Journal of Geophysical Research: Oceans*, *120*, 8439–8465. https://doi.org/10.1002/2015JC010992

Ge, J., Zhou, Z., Yang, W., Ding, P., Chen, C., Wang, Z. B., & Gu, J. (2018). Formation of concentrated benthic suspension in a time-dependent salt wedge estuary. *Journal of Geophysical Research: Oceans*, *123*, 8581–8607. https://doi.org/10.1029/2018JC013876

Guo, L., & He, Q. (2011). Freshwater flocculation of suspended sediments in the Yangtze River, China. *Ocean Dynamics*, *61*(2–3), 371–386. https://doi.org/10.1007/s10236-011-0391-x

Guo, L., Su, N., Zhu, C., & He, Q. (2018). How have the river discharges and sediment loads changed in the Changjiang River basin downstream of the Three Gorges Dam? *Journal of Hydrology*, *560*, 259–274. https://doi.org/10.1016/j.jhydrol.2018.03.035

Guo, W., Wang, X. H., Ding, P., Ge, J., & Song, D. (2018). A system shift in tidal choking due to the construction of Yangshan Harbour, Shanghai, China. *Estuarine, Coastal and Shelf Science*, *206*, 49–60. https://doi.org/10.1016/j.ecss.2017.03.017

Geyer, W. R., Signell, R. P., & Kineke, G. C. (1998). Lateral trapping of sediment in a partially mixed estuary. In J. Dronkers & M. Scheffers (Eds.), *Physics of Estuaries and Coastal Seas: Proceedings of the 8th International Biennial Conference on Physics of Estuaries and Coastal Seas* (pp. 115–124). Balkema.

Hesse, R. F., Zorndt, A., & Fröhle, P. (2019). Modelling dynamics of the estuarine turbidity maximum and local net deposition. *Ocean Dynamics*, *69*(4), 489–507. https://doi.org/10.1007/s10236-019-01250-w

Hu, K., & Ding, P. (2009). The effect of deep waterway constructions on hydrodynamics and salinities in Yangtze Estuary, China. *Journal of Coastal Research*, *II*(56), 961–965.

Hu, K., Ding, P., Wang, Z., & Yang, S. (2009). A 2D/3D hydrodynamic and sediment transport model for the Yangtze Estuary, China. *Journal of Marine Systems*, *77*(1–2), 114–136. https://doi.org/10.1016/j.jmarsys.2008.11.014

Huijts, K. M. H., Schuttelaars, H. M., de Swart, H. E., & Valle-Levinson, A. (2006). Lateral entrapment of sediment in tidal estuaries: An idealized model study. *Journal of Geophysical Research*, *111*, C12016. https://doi.org/10.1029/2006JC003615

Jay, D. A., & Musiak, J. D. (1994). Particle trapping in estuarine tidal flows. *Journal of Geophysical Research*, *99*(C10), 20445. https://doi.org/10.1029/94JC00971

Kim, Y. H., & Voulgaris, G. (2008). Lateral circulation and suspended sediment transport in a curved estuarine channel: Winyah Bay, SC, USA. *Journal of Geophysical Research*, *113*, C09006. https://doi.org/10.1029/2007JC004509

Kristensen, S. E., Drønen, N., Deigaard, R., & Fredsoe, J. (2016). Impact of groyne fields on the littoral drift: A hybrid morphological modelling study. *Coastal Engineering*, *111*, 13–22. https://doi.org/10.1016/j.coastaleng.2016.01.009

Lerczak, J. A., & Geyer, W. R. (2004). Modeling the lateral circulation in straight, stratified estuaries. *Journal of Physical Oceanography*, *34*(6), 1410–1428. https://doi.org/10.1175/1520-0485(2004)034<1410:MTLCIS>2.0.CO;2

Liu, G., Zhu, J., Wang, Y., Wu, H., & Wu, J. (2011). Tripod measured residual currents and sediment flux: Impacts on the silting of the Deepwater Navigation Channel in the Changjiang Estuary. *Estuarine, Coastal and Shelf Science*, *93*(3), 192–201. https://doi.org/10.1016/j.ecss.2010.08.008

Luan, H. L., Ding, P. X., Wang, Z. B., Ge, J. Z., & Yang, S. L. (2016). Decadal morphological evolution of the Yangtze Estuary in response to river input changes and estuarine engineering projects. *Geomorphology*, *265*, 12–23. https://doi.org/10.1016/j.geomorph.2016.04.022

Luan, H. L., Ding, P. X., Wang, Z. B., Yang, S. L., & Lu, J. Y. (2018). Morphodynamic impacts of large-scale engineering projects in the Yangtze River delta. *Coastal Engineering*, *141*, 1–11. https://doi.org/10.1016/j.coastaleng.2018.08.013

McSweeney, J. M., Chant, R. J., & Sommerfield, C. K. (2016). Lateral variability of sediment transport in the Delaware Estuary. *Journal of Geophysical Research: Oceans*, *121*, 725–744. https://doi.org/10.1002/2015JC010974

Nowacki, D. J., & Ganju, N. K. (2018). Storm impacts on hydrodynamics and suspended-sediment fluxes in a microtidal back-barrier estuary. *Marine Geology*, *404*, 1–14. https://doi.org/10.1016/j.margeo.2018.06.016

Officer, C. B. (1981). Physical dynamics of estuarine suspended sediments. *Marine Geology*, *40*(1–2), 1–14. https://doi.org/10.1016/0025-3227(81)90039-6

Ouillon, S., & Dartus, D. (1997). Three-dimensional computation of flow around groyne. *Journal of Hydraulic Engineering*, *123*(11), 962–970. https://doi.org/10.1061/(ASCE)0733-9429(1997)123:11(962)

Postma, H. (1961). Transport and accumulation of suspended matter in the Dutch Wadden Sea. *Netherlands Journal of Sea Research*, *1*(1–2), 148–190. https://doi.org/10.1016/0077-7579(61)90004-7

Postma, H. (1967). Sediment transport and sedimentation in the estuarine environment. In G. H. Lauff (Ed.), *Estuaries*. (pp. 158–179). Washington, DC: American Association for the Advancement of Science.

Ralston, D. K., Geyer, W. R., & Warner, J. C. (2012). Bathymetric controls on sediment transport in the Hudson River estuary: Lateral asymmetry and frontal trapping. *Journal of Geophysical Research*, *117*, C10013. https://doi.org/10.1029/2012JC008124

Scott, T., Austin, M., Masselink, G., & Russell, P. (2016). Dynamics of rip currents associated with groynes-field measurements, modelling and implications for beach safety. *Coastal Engineering*, *107*, 53–69. https://doi.org/10.1016/j.coastaleng.2015.09.013

Simpson, J. H., Brown, J., Matthews, J., & Allen, G. (1990). Tidal straining, density currents, and stirring in the control of estuarine stratification. *Estuaries*, *13*(2), 125. https://doi.org/10.2307/1351581

Song, D., Wang, X. H., Cao, Z., & Guan, W. (2013). Suspended sediment transport in the Deepwater Navigation Channel, Yangtze River Estuary, China, in the dry season 2009: 1. Observations over spring and neap tidal cycles. *Journal of Geophysical Research: Oceans*, *118*, 5555–5567. https://doi.org/10.1002/jgrc.20410

Syvitski, J. P. M. (2005). Impact of humans on the flux of terrestrial sediment to the global coastal ocean. *Science*, *308*(5720), 376–380. https://doi.org/10.1126/science.1109454

Uijttewaal, W. S. J., Lehmann, D., & van Mazijk, A. (2001). Exchange processes between a river and its groyne fields: Model experiments. *Journal of Hydraulic Engineering*, *127*(11), 928–936. https://doi.org/10.1061/(ASCE)0733-9429(2001)127:11(928)

Uncles, R. J., Elliott, R. C. A., & Weston, S. A. (1985a). Lateral distributions of water, salt and sediment transport in a partly mixed estuary. In *Coastal engineering 1984* (pp. 3067–3077). New York, NY: American Society of Civil Engineers. https://doi.org/10.1061/9780872624382.205

Uncles, R. J., Elliott, R. C. A., & Weston, S. A. (1985b). Observed fluxes of water, salt and suspended sediment in a partly mixed estuary. *Estuarine, Coastal and Shelf Science*, *20*(2), 147–167. https://doi.org/10.1016/0272-7714(85)90035-6

van Maren, D. S., van Kessel, T., Cronin, K., & Sittoni, L. (2015). The impact of channel deepening and dredging on estuarine sediment concentration. *Continental Shelf Research*, *95*, 1–14. https://doi.org/10.1016/j.csr.2014.12.010

Walling, D. E., & Fang, D. (2003). Recent trends in the suspended sediment loads of the world's rivers. *Global and Planetary Change*, *39*(1–2), 111–126. https://doi.org/10.1016/S0921-8181(03)00020-1

Wang, Z. B., Van Maren, D. S., Ding, P. X., Yang, S. L., Van Prooijen, B. C., De Vet, P. L. M., et al. (2015). Human impacts on morphodynamic thresholds in estuarine systems. *Continental Shelf Research*, *111*, 174–183. https://doi.org/10.1016/j.csr.2015.08.009

Winterwerp, J. C. (2001). Stratification effects by cohesive and noncohesive sediment. *Journal of Geophysical Research*, *106*(C10), 22559–22574. https://doi.org/10.1029/2000JC000435

Winterwerp, J. C. (2006). Stratification effects by fine suspended sediment at low, medium, and very high concentrations. *Journal of Geophysical Research*, *111*, C05012. https://doi.org/10.1029/2005JC003019

Wood, P. J. (1997). Biological effects of fine sediment in the lotic environment. *Environmental Management*, *21*(2), 203–217. https://doi.org/10.1007/s002679900019

Wu, L., Chen, C., Guo, P., Shi, M., Qi, J., & Ge, J. (2011). A FVCOM-based unstructured grid wave, current, sediment transport model, I. Model description and validation. *Journal of Ocean University of China*, *10*(1), 1–8. https://doi.org/10.1007/s11802-011-1788-3

Yang, S. L., Milliman, J. D., Xu, K. H., Deng, B., Zhang, X. Y., & Luo, X. X. (2014). Downstream sedimentary and geomorphic impacts of the Three Gorges Dam on the Yangtze River. *Earth-Science Reviews*, *138*, 469–486. https://doi.org/10.1016/j.earscirev.2014.07.006

Yang, Z., de Swart, H. E., Cheng, H., Jiang, C., & Valle-Levinson, A. (2014). Modelling lateral entrapment of suspended sediment in estuaries: The role of spatial lags in settling and M4tidal flow. *Continental Shelf Research*, *85*, 126–142. https://doi.org/10.1016/j.csr.2014.06.005

Zheng, L., Chen, C., Alber, M., & Liu, H. (2003). A modeling study of the Satilla River estuary, Georgia. II: Suspended sediment. *Estuaries*, *26*(3), 670–679. https://doi.org/10.1007/BF02711978

Zhou, Z., Ge, J., Wang, Z. B., Maren, D. S., Ma, J., & Ding, P. (2019). Study of lateral flow in a stratified tidal channel-shoal system: The importance of intratidal salinity variation. *Journal of Geophysical Research: Oceans*, *124*, 6702–6719. https://doi.org/10.1029/2019JC015307